Supplementary Material. LRD spectral analysis of multifractional functional time series on manifolds

Diana P. Ovalle–Muñoz[1] · **M. Dolores Ruiz–Medina**[2]

Abstract This Supplementary Material contains a preliminary result on spatiotemporal Karhunen-Loéve expansion to be applied in the proposed estimation approach for SRD–LRD. Some complementary methodological information about generations is also provided. The results obtained in the simulation study undertaken, that are not displayed in Section 5 of the paper, are also included.

1 Preliminary results

In practice, observations are usually collected during a bounded period of time. In the simulation study undertaken in Section 5 of the paper, the generated functional sample lives in $[0, T] \cap \mathbb{Z}$. In this section we consider the separable Hilbert space $\widetilde{H} = L^2(\mathbb{M}_d \times [0, T], d\nu \otimes dt)$ of square integrable functions on $\mathbb{M}_d \times [0, T]$ with respect to the product measure $d\nu \otimes dt$. In particular, $X = \{X(\mathbf{x}, t), \ \mathbf{x} \in \mathbb{M}_d, \ t \in [0, T]\}$ denotes the restriction to $[0, T]$ of a zero–mean, stationary and isotropic mean–square continuous Gaussian, or elliptically contoured, spatiotemporal random field on the basic probability space $(\Omega, \mathcal{A}, P)$, with covariance function

$$
\begin{aligned}
C(d_{\mathbb{M}_d}(\mathbf{x}, \mathbf{y}), t - s) &= \sum_{n \in \mathbb{N}_0} B_n(t - s) \sum_{j=1}^{\delta(n,d)} S_{n,j}^d(\mathbf{x}) S_{n,j}^d(\mathbf{y}) \\
&= \sum_{n \in \mathbb{N}_0} \frac{\delta(n,d)}{\omega_d} B_n(t - s) R_n^{(\alpha,\beta)} \left(\cos\left(d_{\mathbb{M}_d}(\mathbf{x}, \mathbf{y}) \right) \right), \ \mathbf{x}, \mathbf{y} \in \mathbb{M}_d, \ t, s \in [0, T]
\end{aligned}
$$

(1.1)

University of Granada[1,*,2]
Faculty of Sciences, Avd, Fuente Nueva s/n, 18071 Granada, Spain
E-mail: mruiz@ugr.es * corresponding author

(see, e.g., Theorem 4 in Ma and Malyarenko, 2020). This covariance kernel defines the integral operator $\mathcal{C}$ given, for every $f, g \in L^2(\mathbb{M}_d \times [0,T], d\nu \otimes dt)$, by the following identity

$$\mathcal{C}(f)(g) = \int_{\mathbb{M}_d \times \mathbb{M}_d} \int_{[0,T] \times [0,T]} \widetilde{C}(\mathbf{x}, \mathbf{y}, t, s) f(t, \mathbf{x}) g(\mathbf{y}, s) d\nu(\mathbf{x}) d\nu(\mathbf{y}) dt ds. \quad (1.2)$$

Theorem 1 *Let $X = \{X(\mathbf{x}, t), \ \mathbf{x} \in \mathbb{M}_d, \ t \in [0,T]\}$ be the restriction to the interval $[0,T]$ of a zero–mean, stationary and isotropic mean–square continuous Gaussian, or elliptically contoured, spatiotemporal random field on the basic probability space $(\Omega, \mathcal{A}, P)$, with covariance function (1.1) satisfying the conditions in Theorem 4 in Ma and Malyarenko (2020), with*

$$\sum_{n \in \mathbb{N}_0} B_n(0) \delta(n, d) < \infty. \quad (1.3)$$

Then, the following orthogonal expansion holds for random field X

$$X(\mathbf{x}, t) \underset{\mathcal{L}_H^2(\Omega, \mathcal{A}, P)}{=} \sum_{n \in \mathbb{N}_0} \sum_{j=1}^{\delta(n,d)} V_{n,j}(t) S_{n,j}^d(\mathbf{x}), \quad \mathbf{x} \in \mathbb{M}_d, \ t \in [0,T], \quad (1.4)$$

where $\mathcal{L}_{\widetilde{H}}^2(\Omega, \mathcal{A}, P) = L^2(\Omega \times \mathbb{M}_d \times [0,T], P(d\omega) \otimes d\nu \otimes dt)$, with $\widetilde{H} = L^2(\mathbb{M}_d \times [0,T], d\nu \otimes dt)$. Here, $\{V_{n,j}(t), \ t \in [0,T], \ j = 1, \ldots, \delta(n,d), \ n \in \mathbb{N}_0\}$ is a sequence of centered random processes on $[0,T]$ given by

$$V_{n,j}(t) = \int_{\mathbb{M}_d} X(\mathbf{y}, t) S_{n,j}^d(\mathbf{y}) d\nu(\mathbf{y}), \ j = 1, \ldots, \delta(n, d), \ n \in \mathbb{N}_0, \quad (1.5)$$

in the mean–square sense.

Proof Under the conditions of Theorem 4 in Ma and Malyarenko (2020), the spatiotemporal covariance function of X admits the diagonal series expansion given in (1.1). To prove convergence in the mean–square sense of the random series

$$X(\mathbf{x}, t) \underset{\mathcal{L}_{\widetilde{H}}^2(\Omega, \mathcal{A}, P)}{=} \sum_{n \in \mathbb{N}_0} \sum_{j=1}^{\delta(n,d)} V_{n,j}(t) S_{n,j}^d(\mathbf{x}), \quad \mathbf{x} \in \mathbb{M}_d, \ t \in [0,T],$$

$$(1.6)$$

in the space $\widetilde{H} = L^2(\mathbb{M}_d \times [0,T], d\nu \otimes dt)$, we compute for a given $M \geq 2$,

$$E\left[\int_{\mathbb{M}_d \times [0,T]} \left| X(\mathbf{x}, t) - \sum_{n=0}^{M} \sum_{j=1}^{\delta(n,d)} V_{n,j}(t) S_{n,j}^d(\mathbf{x}) \right|^2 d\nu(\mathbf{x}) dt \right]$$

$$= |[0,T]| \sum_{n \in \mathbb{N}_0} B_n(0) \sum_{j=1}^{\delta(n,d)} \int_{\mathbb{M}_d} \left[S_{n,j}^{(d)}(\mathbf{x}) \right]^2 d\nu(\mathbf{x})$$

$$+\sum_{n=0}^{M}\sum_{m=0}^{M}\sum_{j=1}^{\delta(n,d)}\sum_{l=1}^{\delta(m,d)}\int_{\mathbb{M}_d\times[0,T]}E\left[V_{n,j}(t)V_{m,l}(t)\right]S_{n,j}^d(\mathbf{x})S_{m,l}^d(\mathbf{x})d\nu(\mathbf{x})dt$$

$$-2|[0,T]|\sum_{n=0}^{M}\sum_{h=0}^{\infty}B_h(0)\sum_{j=1}^{\delta(n,d)}\sum_{p=1}^{\delta(h,d)}\left[\int_{\mathbb{M}_d}S_{h,p}^d(\mathbf{x})S_{n,j}^d(\mathbf{x})d\nu(\mathbf{x})\right]$$
$$\times\left[\int_{\mathbb{M}_d}S_{h,p}^d(\mathbf{y})S_{n,j}^d(\mathbf{y})d\nu(\mathbf{y})\right]. \qquad (1.7)$$

From equation (1.5),

$$E\left[V_{n,j}(t)V_{m,l}(t)\right]=\int_{\mathbb{M}_d\times\mathbb{M}_d}E\left[X(\mathbf{y},t)X(\mathbf{z},t)\right]S_{m,l}^d(\mathbf{z})S_{n,j}^d(\mathbf{y})d\nu(\mathbf{y})d\nu(\mathbf{z})$$

$$=\int_{\mathbb{M}_d\times\mathbb{M}_d}C(d_{\mathbb{M}_d}(\mathbf{y},\mathbf{z}),0)S_{m,l}^d(\mathbf{z})S_{n,j}^d(\mathbf{y})d\nu(\mathbf{y})d\nu(\mathbf{z})$$

$$=\sum_{h=0}^{\infty}B_h(0)\sum_{p=1}^{\delta(h,d)}\left[\int_{\mathbb{M}_d}S_{h,p}^d(\mathbf{z})S_{m,l}^d(\mathbf{z})d\nu(\mathbf{z})\right]\left[\int_{\mathbb{M}_d}S_{h,p}^d(\mathbf{y})S_{n,j}^d(\mathbf{y})d\nu(\mathbf{y})\right]$$

$$=\delta_{h,m}\delta_{p,l}\delta_{h,n}\delta_{p,j}B_n(0). \qquad (1.8)$$

From equations (1.7) and (1.8), applying orthonormality of the basis $\left\{S_{n,j}^d,\ j=1,\ldots,\delta(n,d),\ n\in\mathbb{N}_0\right\}$, we obtain as $M\to\infty$,

$$E\left[\int_{\mathbb{M}_d\times[0,T]}\left|X(\mathbf{x},t)-\sum_{n=0}^{M}\sum_{j=1}^{\delta(n,d)}V_{n,j}(t)S_{n,j}^d(\mathbf{x})\right|^2d\nu(\mathbf{x})dt\right]$$

$$=|[0,T]|\left[\sum_{n\in\mathbb{N}_0}B_n(0)\delta(n,d)+\sum_{n=0}^{M}B_n(0)\delta(n,d)-2\sum_{n=0}^{M}B_n(0)\delta(n,d)\right]\to 0,$$

as we wanted to prove.

Remark 1 Note that condition $\sum_{n\in\mathbb{N}_0}B_n(0)\delta(n,d)<\infty$ implies from Cauchy–Schwartz inequality,

$$=\int_0^T\int_0^T\int_{\mathbb{M}_d\times\mathbb{M}_d}|E\left[X(\mathbf{x},t)X(\mathbf{y},s)\right]|^2d\nu(\mathbf{x})d\nu(\mathbf{y})dtds$$
$$\leq|T|^2\sum_{n\in\mathbb{N}_0}\delta(n,d)[B_n(0)]^2<\infty. \qquad (1.9)$$

That is, integral operator $\mathcal{C}$ in equation (1.2) belongs to the space $\mathcal{S}\left(L^2(\mathbb{M}_d\times[0,T],d\nu\otimes dt)\right)$ of Hilbert–Schmidt operators on $L^2(\mathbb{M}_d\times[0,T],d\nu\otimes dt)$.

1.1 Complementary theoretical information about the simulation study

Let us consider the following random field model

$$Y_{\mathbf{U}}(\mathbf{x}, t) = \frac{1}{\sqrt{\omega_d}} \sum_{n \in \mathbb{N}_0} V_n(t) \sum_{j=1}^{\delta(n,d)} S_{n,j}^{(d)}(\mathbf{x}) S_{n,j}^{(d)}(\mathbf{U}) \tag{1.10}$$

$$= \sum_{n \in \mathbb{N}_0} V_n(t) \frac{\delta(n,d) R_n^{(\alpha,\beta)} \left(\cos \left(d_{\mathbb{M}_d}(\mathbf{x}, \mathbf{U}) \right) \right)}{\omega_d \sqrt{\omega_d}}, \tag{1.11}$$

where $\mathbf{U}$ represents a uniform random variable with values in the manifold $\mathbb{M}_d$ independent of the centered temporal random coefficients $\{V_n(t), \ t \in [0,T], \ n \in \mathbb{N}_0,\}$ satisfying $E[V_n(t)V_m(s)] = \delta_{n,m} B_n(t-s)$, $t, s \in [0,T]$, $n, m \in \mathbb{N}_0$.

From equation (1.10), applying again orthonormality of the basis $\left\{ S_{n,j}^d, \ j = 1, \ldots, \delta(n,d), \ n \in \mathbb{N}_0 \right\}$, the covariance function of $Y_{\mathbf{U}}$ is given by

$$E\left[Y_{\mathbf{U}}(\mathbf{x}, t) Y_{\mathbf{U}}(\mathbf{y}, s) \right] = \frac{1}{\omega_d} \sum_{n \in \mathbb{N}_0} \sum_{m \in \mathbb{N}_0} E\left[V_n(t) V_m(s) \right]$$

$$\times \sum_{j=1}^{\delta(n,d)} \sum_{l=1}^{\delta(m,d)} E\left[S_{n,j}^{(d)}(\mathbf{U}) S_{m,l}^{(d)}(\mathbf{U}) \right] S_{n,j}^{(d)}(\mathbf{x}) S_{m,l}^{(d)}(\mathbf{y})$$

$$= \sum_{n \in \mathbb{N}_0} B_n(t-s) \frac{\delta(n,d)}{\omega_d} R_n^{(\alpha,\beta)} \left(\cos \left(d_{\mathbb{M}_d}(\mathbf{x}, \mathbf{y}) \right) \right), \quad \mathbf{x}, \mathbf{y} \in \mathbb{M}_d, \ t, s \in [0,T], \tag{1.12}$$

which coincides with the covariance function (1.1) of random field X. Thus, the two spatiotemporal random fields, X and $Y_{\mathbf{U}}$, are characterized by the same spatiotemporal Reproducing Kernel Hilbert Space (RKHS) $\mathcal{H} = \mathcal{C}^{1/2}(\widetilde{H})$, with $\mathcal{C}^{1/2}$ being the square root of integral operator $\mathcal{C}$ introduced in (1.2). Its dual Hilbert space $\mathcal{H}^{\star}$ is characterized by the inner product

$$\langle f, g \rangle_{\mathcal{H}^{\star}} = \sum_{n \in \mathbb{N}_0} \sum_{j=1}^{\delta(n,d)} \int_{[0,T] \times [0,T]} f_{n,j}(t) g_{n,j}(s) B_n(t-s) dt ds,$$

with $f_{n,j}(t) = \left\langle f(\cdot, t), S_{n,j}^{(d)} \right\rangle_{L^2(\mathbb{M}_d, d\nu)}$, and $g_{n,j}(s) = \left\langle g(\cdot, s), S_{n,j}^{(d)} \right\rangle_{L^2(\mathbb{M}_d, d\nu)}$, for every $f, g \in \widetilde{H}$, and $t, s \in [0,T]$. Hence, these two random fields belong to the same equivalence class, characterized by the RKHS, isometrically identified with the linear closed span in $\mathcal{L}^2(\Omega, \mathcal{A}, P)$ of the random variables of X.

Since the two proposed estimation methodologies are based on the second–order moment information in the functional spectral domain, one can perform the illustration of their performance from any element of the equivalence class of X. In particular, we have chosen random field $Y_{\mathbf{U}}$, having the same family of covariance and spectral density operators as X in the functional time series

framework. Specifically, if **Condition C0**, in particular, equation (3.1) is satisfied by random field (RF) X, then RF $Y_{\mathbf{U}}$ also satisfies this condition. Thus, equation (3.3) in the paper holds for both RFs, X and $Y_{\mathbf{U}}$, leading to Theorem 1 is also satisfied by both RFs. Moreover, if **Condition C1** is satisfied by RF X, then, this condition is also satisfied by $Y_{\mathbf{U}}$ having the same spectral density operator family. Conclusions derived from the empirical analysis achieved in Section 5.1 on minimum contrast parameter estimation methodology, based on the empirical errors and empirical probabilities (see also Section 4 below), are based on generations of random field $Y_{\mathbf{U}}$ beyond the Gaussian scenario.

Finally, we recall that when the projected process displays SRD and LRD depending on the spherical scale, the weighted periodogram operator estimation has been applied for approximation of SRD functional spectral factor. Theorem 3.6 in Panaretos and Tavakoli (2013) proves consistency in the mean–square sense in the norm of the space $\mathcal{S}(L^2(\mathbb{M}_d, d\nu, \mathbb{C}))$ holds, that is, consistency is satisfied in $\mathcal{L}_{\mathcal{S}(L^2(\mathbb{M}_d, d\nu, \mathbb{C}))}(\Omega, \mathcal{A}, P)$. Note that condition (3.1) leads to equation (3.3) of the paper, ensuring that Theorems 1 and 2 also hold. Applying the equivalent asymptotic behavior of the projected weighted periodogram operator estimators from both RFs, X and $Y_{\mathbf{U}}$, the results displayed in Section 5.2 of the paper, based on generations of functional samples of random field $Y_{\mathbf{U}}$, illustrate weak–consistency beyond the Gaussian scenario (see also Section 5 below).

2 Parametric scenarios analyzed in the simulation study

Table 1: True parameters for decreasing and nondecreasing LRD operator eigenvalues

Case	Definition
Decreasing eigenvalue sequence	$\alpha(n, \theta_0) = 0.4063 - \dfrac{1}{3.6} \left[\left(\theta_{0,1} + \theta_{0,2}n + \theta_{0,3}n^2\right) / \theta_{0,4}(n) \right],$ $n = 1, \ldots, 30.$ $\theta_{0,1} = 0.75, \ \theta_{0,2} = 0.76, \ \theta_{0,3} = 0.77$ $\theta_{0,4}(n) = \|f_n(i)\|_\infty = \sup_{i=1,\ldots,100} f_n(i)$ $f_n(i) = i/100 + ((i+1)/100)n + ((i+2)/100)n^2.$
Nondecreasing eigenvalue sequence	$\alpha(n, \vartheta_0) = \dfrac{1}{10} \left[\dfrac{\exp(-(\vartheta_{0,2} + \vartheta_{0,3}n))}{\vartheta_{0,1}} + 1 \right], \ n = 1, \ldots, 30.$ $\vartheta_0 = (\vartheta_{0,1}, \vartheta_{0,2}, \vartheta_{0,3}) = (-9, 1, 1).$

Table 2: Candidates for LRD operator decreasing and nondecreasing eigenvalue sequence

Case	Definition
Decreasing eigenvalue sequence	$\alpha(n, \theta_i) = 0.4 - \dfrac{1}{3.6} \left[\left(\theta_{i,1} + \theta_{i,2}n + \theta_{i,3}n^2\right) / \theta_{0,4}(n) \right],$ $n = 1, \ldots, 30$ $\theta_{i,1} = i/100, \ \theta_{i,2} = (i+1)/100, \ \theta_{i,3} = (i+2)/100, \ i = 1, \ldots, 100.$
Nondecreasing eigenvalue sequence	$\alpha(n, \vartheta_i) = \dfrac{1}{10} \left[\dfrac{\exp(-(\vartheta_{i,2} + \theta_{i,3}n))}{\vartheta_{i,1}} + 1 \right], n = 1, \ldots, 30$ $\vartheta_i = (\vartheta_{i,1}, \vartheta_{i,2}, \theta_{i,3}) = \left(-70, 1 + \dfrac{i}{100}, 1 + \dfrac{i+1}{100} \right), \ i = 1, \ldots, 100.$

Table 3: Parameter values in the SPHARMA(p,q) generations

Model	Definition
SPHAR(1)	$$\Phi_1(\mathbf{x}, \mathbf{y}) = \sum_{n \in \mathbb{N}_0} \lambda_n(\Phi_1) \sum_{j=1}^{\delta(n,d)} S_{n,j}^d(\mathbf{x}) S_{n,j}^d(\mathbf{y})$$ $$\lambda_n(\Phi_1) = (0.7(n+1/n))^{-3/2}$$ $$\sigma_n^2 = (0.015(n/(n+1)))^{-3/2}, \ n = 1, \ldots, 30.$$
SPHAR(3)	$$\Phi_i(\mathbf{x}, \mathbf{y}) = \sum_{n \in \mathbb{N}_0} \lambda_n(\Phi_i) \sum_{j=1}^{\delta(n,d)} S_{n,j}^d(\mathbf{x}) S_{n,j}^d(\mathbf{y}), \ i = 1,2,3$$ $$\lambda_n(\Phi_1) = 0.6((n+1)/n)^{-3/2}, \ \lambda_n(\Phi_2) = 0.2((n+1)/n)^{-3/2}$$ $$\lambda_n(\Phi_3) = 0.1((n+1)/n)^{-3/2}$$ $$\sigma_n^2 = (0.01(n/(n+1)))^{-3/2}, \ n = 1, \ldots, 30.$$
SPHARMA(1,1)	$$\Phi_1(\mathbf{x}, \mathbf{y}) = \sum_{n \in \mathbb{N}_0} \lambda_n(\Phi_1) \sum_{j=1}^{\delta(n,d)} S_{n,j}^d(\mathbf{x}) S_{n,j}^d(\mathbf{y})$$ $$\Psi_1(\mathbf{x}, \mathbf{y}) = \sum_{n \in \mathbb{N}_0} \lambda_n(\Psi_1) \sum_{j=1}^{\delta(n,d)} S_{n,j}^d(\mathbf{x}) S_{n,j}^d(\mathbf{y})$$ $$\lambda_n(\Phi_1) = (0.7(n+1/n))^{-3/2}$$ $$\lambda_n(\Psi_1) = 0.4(n+1/n)^{-3/2}$$ $$\sigma_n^2 = (0.015(n/(n+1)))^{-3/2}, \ n = 1, \ldots, 30.$$
SPHARMA(3,1)	$$\Phi_i(\mathbf{x}, \mathbf{y}) = \sum_{n \in \mathbb{N}_0} \lambda_n(\Phi_i) \sum_{j=1}^{\delta(n,d)} S_{n,j}^d(\mathbf{x}) S_{n,j}^d(\mathbf{y}), \ i = 1,2,3$$ $$\Psi_1(\mathbf{x}, \mathbf{y}) = \sum_{n \in \mathbb{N}_0} \lambda_n(\Psi_1) \sum_{j=1}^{\delta(n,d)} S_{n,j}^d(\mathbf{x}) S_{n,j}^d(\mathbf{y})$$ $$\lambda_n(\Phi_1) = 0.5((n+1)/n)^{-3/2}, \ \lambda_n(\Phi_2) = 0.3((n+1)/n)^{-3/2}$$ $$\lambda_n(\Phi_3) = 0.2((n+1)/n)^{-3/2}, \lambda_n(\Psi_1) = 0.4((n+1)/n)^{-3/2}$$ $$\sigma_n^2 = (0.015(n/n+1))^{-3/2}, \ n = 1, \ldots, 30.$$

3 Sample path generations

Multifractionally integrated SPHAR(3) process under nondecreasing eigen-value sequence of the LRD operator is displayed in Figure 1 (see Figure 3 of the paper for LRD operator decreasing eigenvalue sequence). Figures 2, 3 and 4 respectively show the generations of the multifractionally integrated SPHAR(1), SPHARMA(1,1), and SPHARMA(3,1) processes, under LRD operator decreasing eigenvalue sequence for truncation order $M = 10$, and under nondecreasing eigenvalue sequence of the LRD operator for truncation order $M = 6$.
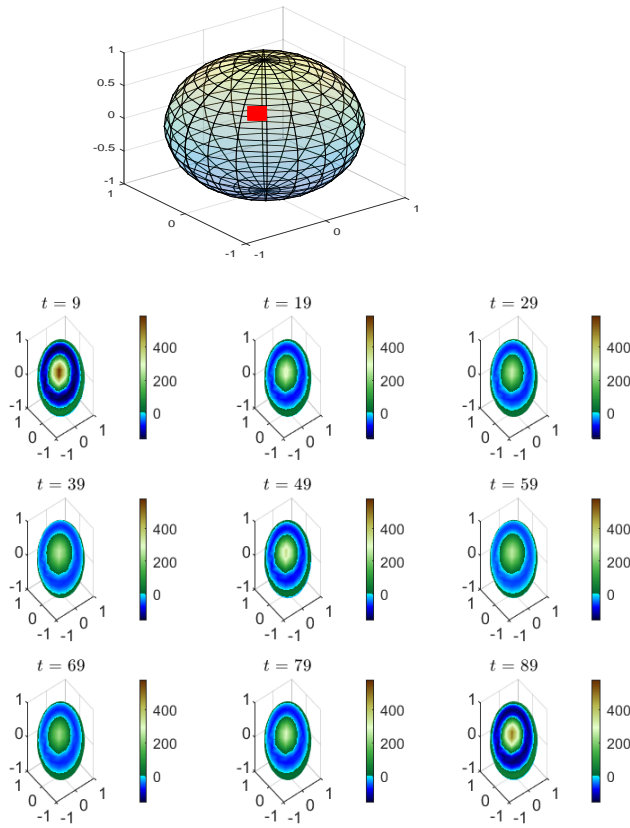
Fig. 1: At the top, pole $\mathbf{U} = \mathbf{u}_0$ considered in the zonal functions involved in the generations. At the bottom, generations of multifractionally integrated SPHAR(3) process $\widetilde{X}$ at times $t = 9, 19, 29, 39, 49, 59, 69, 79, 89$, projected into the direct sum of eigenspaces H_n, $n = 1, \ldots, 6$, of the Laplace Beltrami operator on $L^2(\mathbb{S}_2, d\nu)$, under LRD operator nondecreasing eigenvalue sequence

Fig. 2: At the top, generations of multifractionally integrated SPHAR(1) process $\widetilde{X}$ at times $t = 9, 19, 29, 39, 49, 59, 69, 79, 89$, projected into the direct sum of eigenspaces H_n, $n = 1, \dots, 10$, of the Laplace Beltrami operator on $L^2(\mathbb{S}_2, d\nu)$, under LRD operator decreasing eigenvalue sequence. At the bottom, generations of multifractionally integrated SPHAR(1) process $\widetilde{X}$ at times $t = 9, 19, 29, 39, 49, 59, 69, 79, 89$, projected into the direct sum of eigenspaces H_n, $n = 1, \dots, 6$, of the Laplace Beltrami operator on $L^2(\mathbb{S}_2, d\nu)$, under LRD operator nondecreasing eigenvalue sequence

Fig. 3: At the top, generations of multifractionally integrated SPHARMA(1,1) process $\widetilde{X}$ at times $t = 9, 19, 29, 39, 49, 59, 69, 79, 89$, projected into the direct sum of eigenspaces H_n, $n = 1, \ldots, 10$, of the Laplace Beltrami operator on $L^2(\mathbb{S}_2, d\nu)$, under LRD operator decreasing eigenvalue sequence. At the bottom, generations of multifractionally integrated SPHARMA(1,1) process $\widetilde{X}$ at times $t = 9, 19, 29, 39, 49, 59, 69, 79, 89$, projected into the direct sum of eigenspaces H_n, $n = 1, \ldots, 6$, of the Laplace Beltrami operator on $L^2(\mathbb{S}_2, d\nu)$, under LRD operator nondecreasing eigenvalue sequence
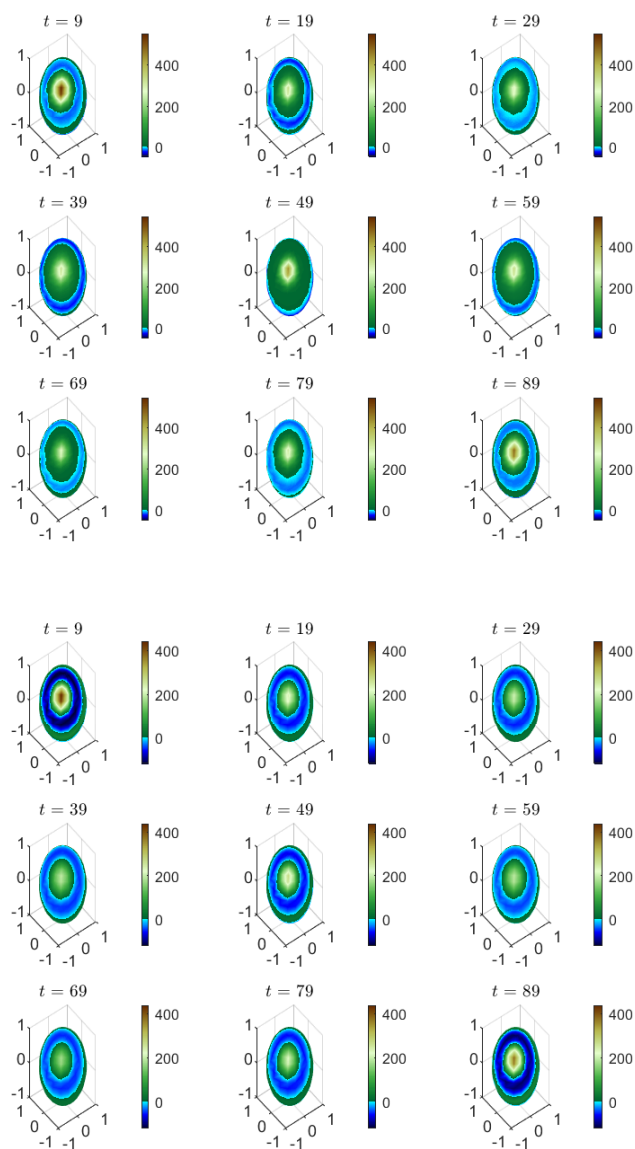
Fig. 4: At the top, generations of multifractionally integrated SPHARMA(3,1) process $\widetilde{X}$ at times $t = 9, 19, 29, 39, 49, 59, 69, 79, 89$, projected into the direct sum of eigenspaces H_n, $n = 1, \ldots, 10$, of the Laplace Beltrami operator on $L^2(\mathbb{S}_2, d\nu)$, under LRD operator decreasing eigenvalue sequence. At the bottom, generations of multifractionally integrated SPHARMA(3,1) process $\widetilde{X}$ at times $t = 9, 19, 29, 39, 49, 59, 69, 79, 89$, projected into the direct sum of eigenspaces H_n, $n = 1, \ldots, 6$, of the Laplace Beltrami operator on $L^2(\mathbb{S}_2, d\nu)$, under LRD operator nondecreasing eigenvalue sequence
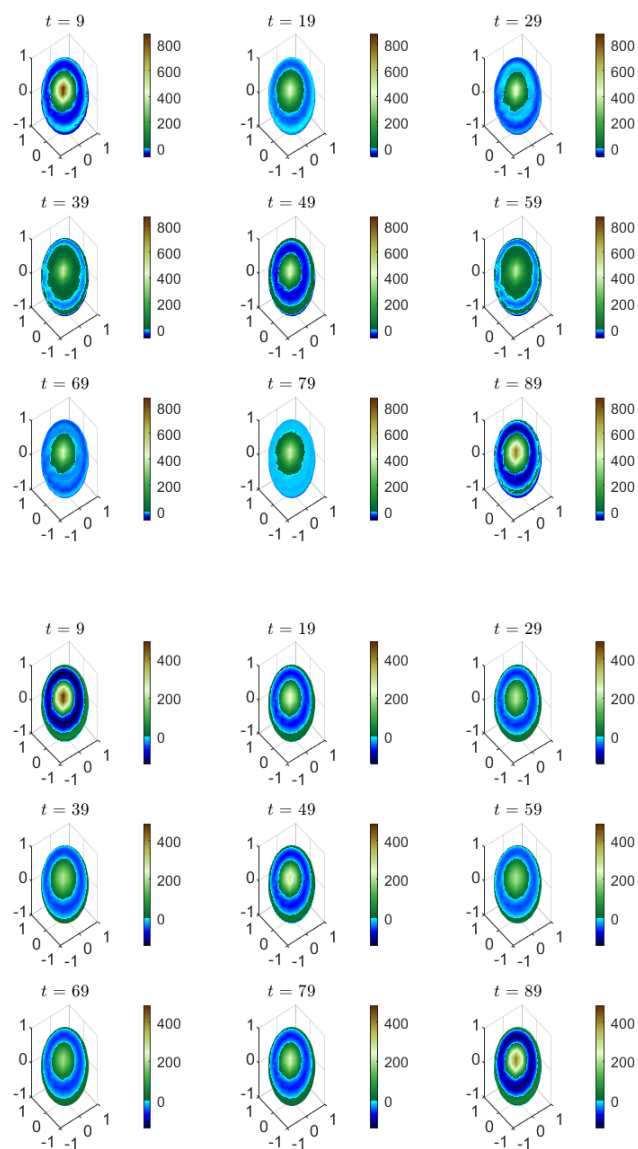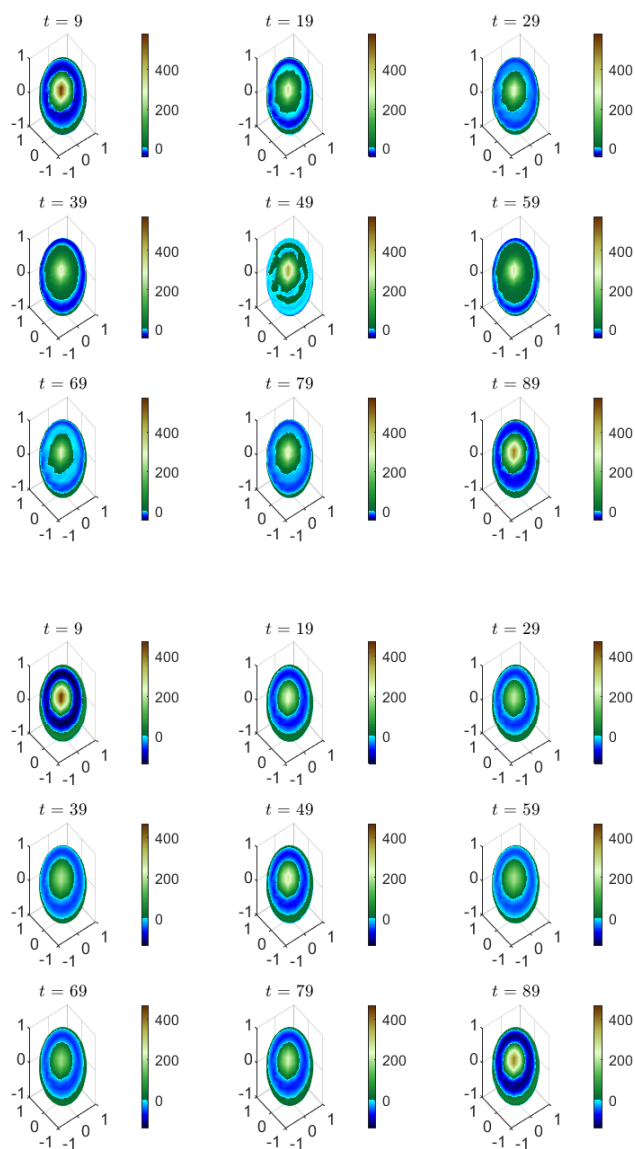
3.1 Multifractionally integrated SPHARMA(1,1) processes displaying SRD and LRD

Generations of the special case where the projected process into the eigenspace H_n, $n = 1, \ldots, 15$, of the spherical Laplace Beltrami operator displays LRD, and SRD for $n = 16, \ldots, 30$, are now displayed for the multifractionally integrated SPHARMA(1,1) process family.
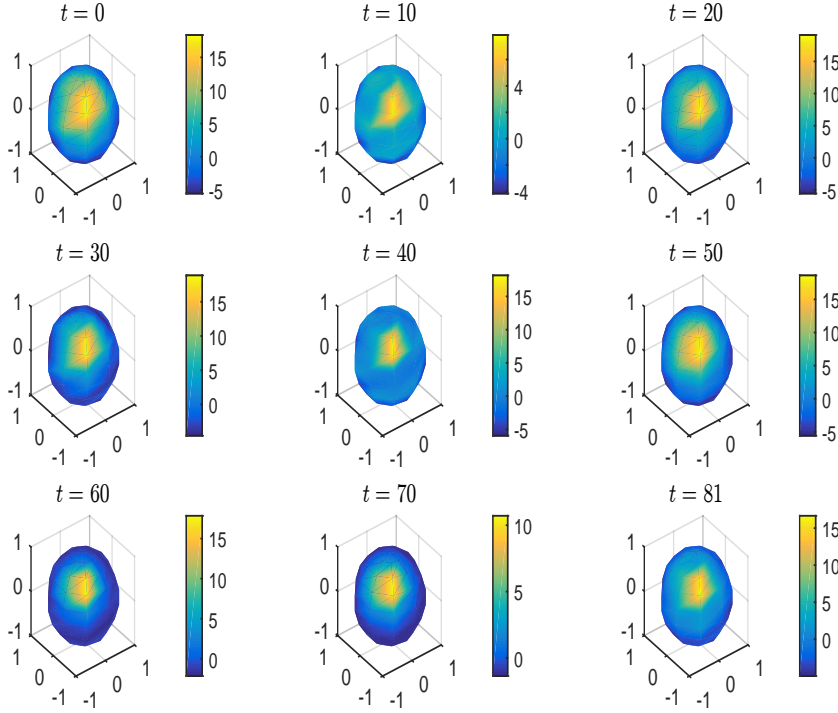
Fig. 5: The generated multifractionally integrated SPHARMA(1,1) for times $t = 0, 10, 20, 30, 40, 50, 60, 70, 81$, under a LRD and SRD scenarios

4 Empirical analysis of minimum contrast estimation

This section illustrates the performance of the minimum contrast estimation methodology introduced in Section 3 of the paper. The empirical analysis, based on the empirical distribution of the temporal mean of the empirical absolute errors, and the empirical probabilities, is achieved from $R = 100, 2000, 5000$ independent generations of each one of the functional samples of size $T = 50, 500, 1000$ considered. In all the models analyzed, within the family of multifractionally integrated SPHAR(p), $p = 1, 3$, and SPHARMA(p,q),

$p = 1, 3$ and $q = 1$ processes, the scenarios corresponding to decreasing and nondecreasing eigenvalue sequence of the LRD operator are tested.

4.1 Multifractionally integrated SPHAR(1) process under LRD operator decreasing eigenvalues

Figures 6–8 show the histograms of the temporal mean of the empirical absolute errors, obtained in the implementation of the minimum contrast estimation methodology, from $R = 100, 2000, 5000$ independent generations of each one of the functional samples of size $T = 50, 500, 1000$ of multifractionally integrated SPHAR(1) process. Specifically, plots display in all the cases the results for the projected process into the eigenspaces H_n, $n = 1, 5, 10, 15, 20, 25, 30$, of the spherical Laplace Beltrami operator. The same functional sample sizes and repetitions have been considered in the computation of the empirical probabilities

$$\widehat{\mathcal{P}} \left(\|f_{n,\theta_0}(\cdot) - f_{n,\widehat{\theta}_T}(\cdot)\|_{L^1([-\pi,\pi])} > \varepsilon_i \right), \ i = 1, \ldots, 100, \qquad (4.13)$$

where, as before, they are displayed in the considered 30 spatial spherical scales, and for a grid of 100 thresholds in the interval $(0, 0.1)$ (see Figure 9).

4.2 Multifractionally integrated SPHAR(1) process under LRD operator nondecreasing eigenvalues

Figures 10–12, and 13 respectively show the histograms of the temporal mean of the empirical absolute errors, and the empirical probabilities (4.13) obtained from a grid of 100 thresholds in the interval $(0, 0.1)$, based on $R = 100, 2000, 5000$ repetitions of each one of the functional samples of size $T = 50, 500, 1000$. As before, Figures 10–12 display projections into the eigenspaces $n = 10, 15, 20, 25, 30$ of the Laplace Beltrami operator, and plots in Figure 13 show empirical probabilities (4.13) for all $n \in \{1, \ldots, 30\}$.

4.3 Multifractionally integrated SPHAR(3) process under LRD operator decreasing eigenvalues

Figures 14–15 show the histograms of the temporal mean of the empirical absolute errors, obtained in the implementation of the minimum contrast estimation methodology, from $R = 100, 2000, 5000$ independent realizations of each one of the functional samples of sizes $T = 50, 500$ of the generated SPHAR(3) process. Plots display the results for projections into the eigenspaces H_n, $n = 1, 5, 10, 15, 20, 25, 30$, of the Laplace Beltrami operator.

(a) $R = 100$, scales 1–5 (b) $R = 2000$, scales 1–5 (c) $R = 5000$, scales 1–5

(d) $R = 100$, scales 10–15 (e) $R = 2000$, scales 10–15 (f) $R = 5000$, scales 10–15

(g) $R = 100$, scales 20–25 (h) $R = 2000$, scales 20–25 (i) $R = 5000$, scales 20–25

(j) $R = 100$, scales 25–30 (k) $R = 2000$, scales 25–30 (l) $R = 5000$, scales 25–30

Fig. 6: Histograms of the temporal mean of the empirical absolute errors, for the sample size $T = 50$ (LRD operator decreasing eigenvalues, multifractionally integrated SPHAR(1) process)

4.4 Multifractionally integrated SPHAR(3) process under LRD operator nondecreasing eigenvalues

Figures 16–18 show the histograms of the temporal mean of the empirical absolute errors, based on $R = 100, 2000, 5000$ independent generations of each one of the functional samples of size $T = 50, 500, 1000$, of multifractionally integrated SPHAR(3) process considered. As before, Figures 16–18 display the results for the projections into the eigenspaces $n = 10, 15, 20, 25, 30$ of the spherical Laplace Beltrami operator.

(a) $R = 100$, scales 1–5 (b) $R = 2000$, scales 1–5 (c) $R = 5000$, scales 1–5

(d) $R = 100$, scales 10–15 (e) $R = 2000$, scales 10–15 (f) $R = 5000$, scales 10–15

(g) $R = 100$, scales 20–25 (h) $R = 2000$, scales 20–25 (i) $R = 5000$, scales 20–25

(j) $R = 100$, scales 25–30 (k) $R = 2000$, scales 25–30 (l) $R = 5000$, scales 25–30

Fig. 7: Histograms of the temporal mean of the empirical absolute errors, for the sample size $T = 500$ (LRD operator decreasing eigenvalues, multifractionally integrated SPHAR(1) process)

4.5 Multifractionally integrated SPHARMA(1,1) process under LRD operator decreasing eigenvalues

Figures 19–21 show the histograms of the temporal mean of the empirical absolute errors based on $R = 100, 2000, 5000$ independent generations of each one of the functional samples of size $T = 50, 500, 1000$ of multifractionally integrated SPHARMA(1,1) model, obtained from projection into the eigenspaces $n = 1, 5, 10, 15, 20, 25, 30$ of the spherical Laplace Beltrami operator. The same functional sample sizes and repetitions have been considered in the computa-

(a) $R = 100$, scales 1–5   (b) $R = 2000$, scales 1–5   (c) $R = 5000$, scales 1–5

(d) $R = 100$, scales 10–15   (e) $R = 2000$, scales 10–15   (f) $R = 5000$, scales 10–15

(g) $R = 100$, scales 20–25   (h) $R = 2000$, scales 20–25   (i) $R = 5000$, scales 20–25

(j) $R = 100$, scales 25–30   (k) $R = 2000$, scales 25–30   (l) $R = 5000$, scales 25–30
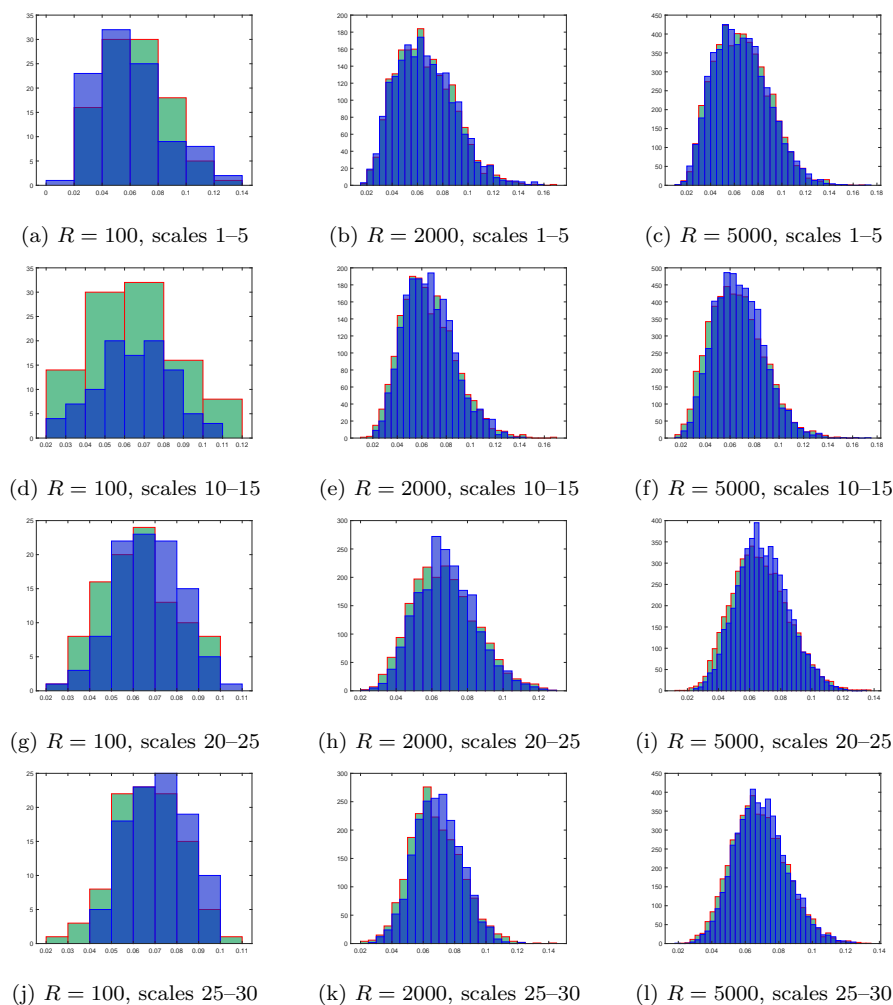
Fig. 8: Histograms of the temporal mean of the empirical absolute errors, for the sample size $T = 1000$ (LRD operator decreasing eigenvalues, multifractionally integrated SPHAR(1) process)

tion of the empirical probabilities (4.13), where, as before, they are displayed in the 30 spatial spherical scales, and for a grid of 100 thresholds in the interval $(0, 0.1)$ (see Figure 22).

(a) $T = 50, R = 100$ (b) $T = 50, R = 2000$ (c) $T = 50, R = 5000$

(d) $T = 500, R = 100$ (e) $T = 500, R = 2000$ (f) $T = 500, R = 5000$

(g) $T = 1000, R = 100$ (h) $T = 1000, R = 2000$ (i) $T = 1000, R = 5000$
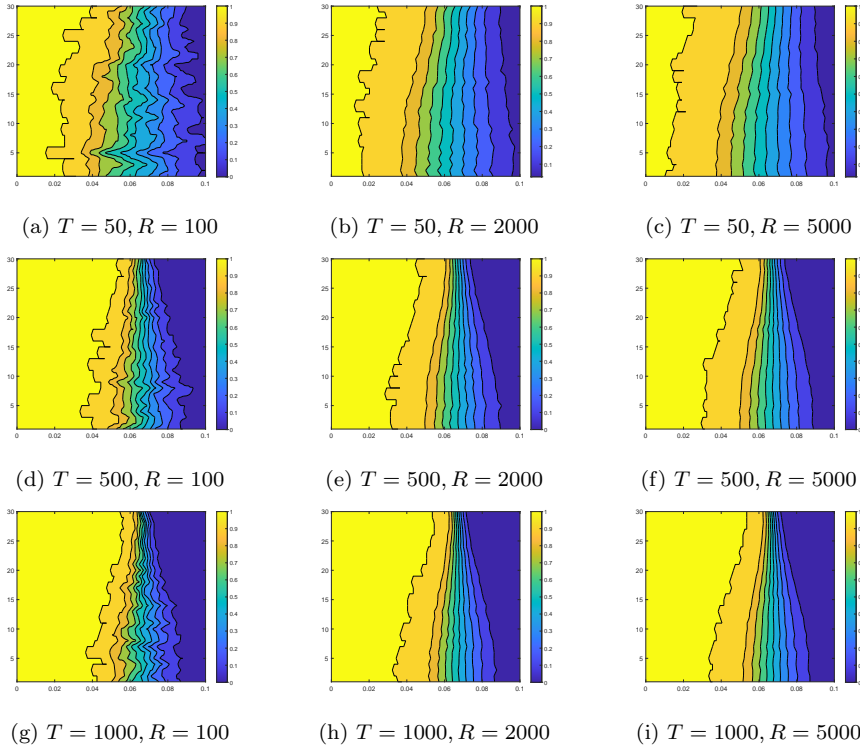
Fig. 9: Empirical probabilities in equation (4.13) (decreasing LRD operator eigenvalues, multifractionally integrated SPHAR(1) process)

4.6 Multifractionally integrated SPHARMA(1,1) process under LRD operator nondecreasing eigenvalues

Figures 23–25, and 26 respectively show the histograms of the temporal mean of the empirical absolute errors, and the empirical probabilities (4.13) obtained from a grid of 100 thresholds in the interval $(0, 0.1)$, based on $R = 100, 2000, 5000$ independent generations of each one of the functional samples of size $T = 50, 500, 1000$ of multifractionally integrated SPHARMA(1,1) process. As before, Figures 23–25 display projections into the eigenspaces $n = 10, 15, 20, 25, 30$ of the Laplace Beltrami operator, and plots in Figure 26 show empirical probabilities (4.13) for all $n \in \{1, \ldots, 30\}$.

4.7 Multifractionally integrated SPHARMA(3,1) process under LRD operator decreasing eigenvalues

Figures 27–29 show the histograms of the temporal mean of the empirical absolute errors based on $R = 100, 2000, 5000$ independent generations of each

(a) $R = 100$, scales 10–15   (b) $R = 2000$, scales 10–15   (c) $R = 5000$, scales 10–15

(d) $R = 100$, scales 20–25   (e) $R = 2000$, scales 20–25   (f) $R = 5000$, scales 20–25

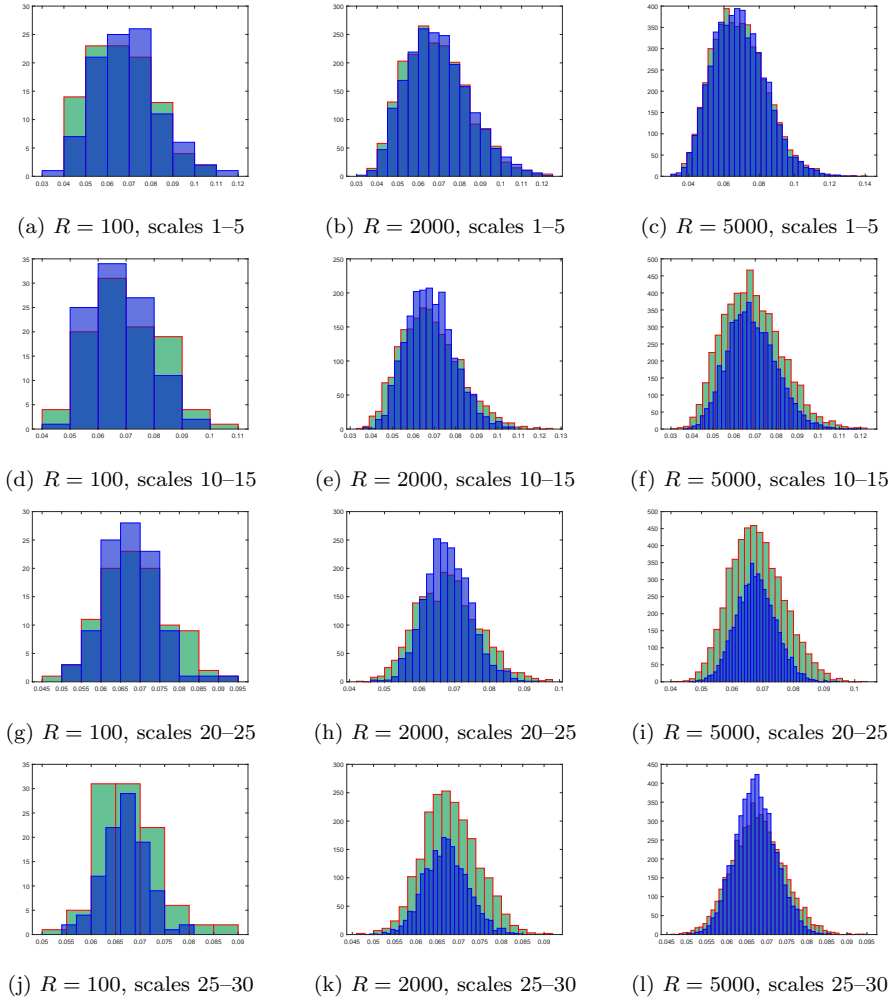(g) $R = 100$, scales 25–30   (h) $R = 2000$, scales 25–30   (i) $R = 5000$, scales 25–30

Fig. 10: Histograms of the temporal mean of the empirical absolute errors, for the sample size $T = 50$ (LRD operator nondecreasing eigenvalues, multifractionally integrated SPHAR(1) process)

one of the functional samples of size $T = 50, 500, 1000$, of multifractionally integrated SPHARMA(3,1) process. The histograms are displayed for approximations into the eigenspaces $n = 1, 5, 10, 15, 20, 25, 30$ of the spherical Laplace Beltrami operator. The same functional samp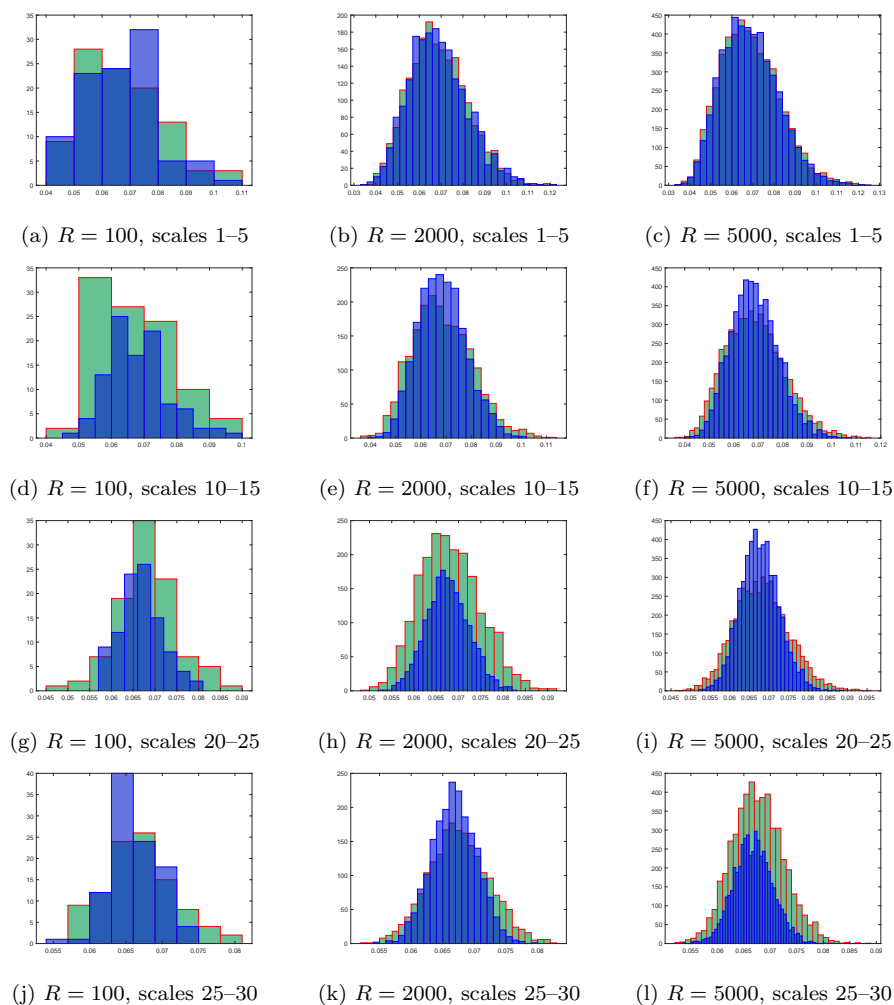le sizes and repetitions have been considered in the computation of the empirical probabilities (4.13), where, as before, they are displayed in the 30 analyzed spatial spherical scales, and for a grid of 100 thresholds in the interval $(0, 0.1)$ (see Figure 30).

4.8 Multifractionally integrated SPHARMA(3,1) process under nondecreasing LRD operator scenario

Generations of the multifractionally integrated SPHARMA(3,1) process are now considered, in the implementation of the minimum contrast estimation methodology, under LRD operator nondecreasing eigenvalues. Figures 31–33, and 34 respectively show the histograms of the temporal mean of the empirical absolute errors, and the empirical probabilities (4.13) obtained from a grid of

(a) $R = 100$, scales 10–15   (b) $R = 2000$, scales 10–15   (c) $R = 5000$, scales 10–15

(d) $R = 100$, scales 20–25   (e) $R = 2000$, scales 20–25   (f) $R = 5000$, scales 20–25

(g) $R = 100$, scales 25–30   (h) $R = 2000$, scales 25–30   (i) $R = 5000$, scales 25–30

Fig. 11: Histograms of the temporal mean of the empirical absolute errors, for the sample size $T = 500$ (LRD operator nondecreasing eigenvalues, multifractionally integrated SPHAR(1) process)

100 thresholds in the interval $(0, 0.1)$, from $R = 100, 2000, 5000$, independent generations of each one of the functional samples of size $T = 50, 500, 1000$ of multifractionally integrated SPHARMA(3,1) model. As before, Figures 31–33 display projections into the eigenspaces $n = 10, 15, 20, 25, 30$ of the spherical Laplace Beltrami operator, and plots in Figure 34 show empirical probabilities (4.13) for all $n \in \{1, \dots, 30\}$.

5 Empirical analysis of SRD–LRD estimation

This section provides the empirical analysis, based on $R = 100$ independent generations of each one of the functional samples of size $T = 50, 100, 500, 1000$ (of multifractionally integrated (M.I.) SPHAR(1), SPHAR(3), SPHARMA(1,1), SPHARMA(3,1) processes), achieved from the empirical mean quadratic errors (E.M.Q.E.s) of the functional estimation of SRD spectral operator, based on the projected weighted periodogram operator (P.W.P.O.) for $n = 16, \dots, 30$ (left–hand side of Figures 35–38). It is well-known that the bandwidth param-

(a) $R = 100$, scales 10–15   (b) $R = 2000$, scales 10–15   (c) $R = 5000$, scales 10–15

(d) $R = 100$, scales 20–25   (e) $R = 2000$, scales 20–25   (f) $R = 5000$, scales 20–25

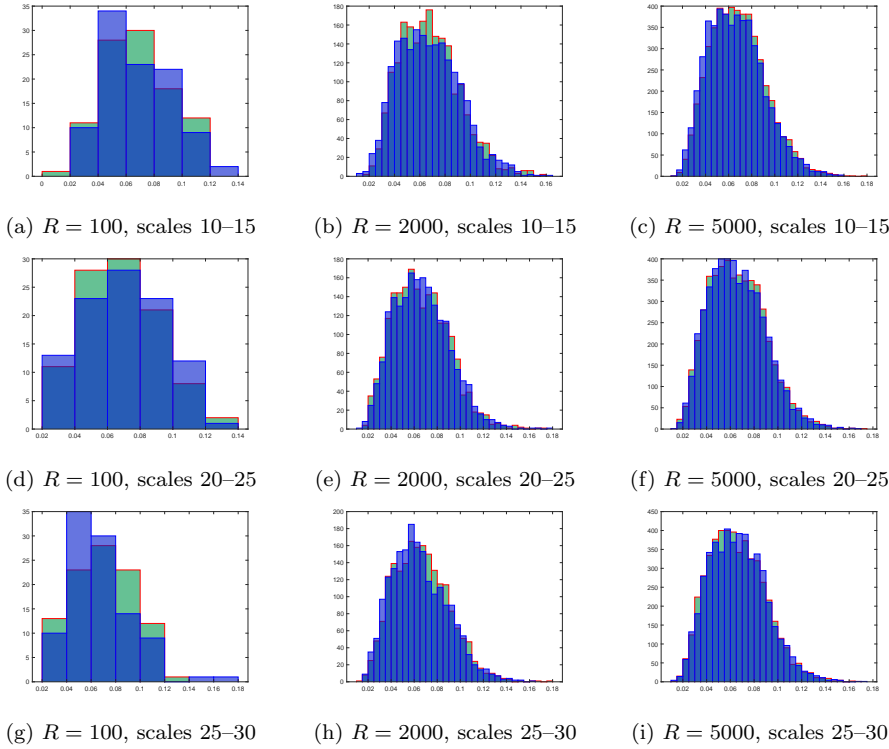(g) $R = 100$, scales 25–30   (h) $R = 2000$, scales 25–30   (i) $R = 5000$, scales 25–30

Fig. 12: Histograms of the temporal mean of the empirical absolute errors, for the sample size $T = 1000$ (LRD operator nondecreasing eigenvalues, multi-fractionally integrated SPHAR(1) process)

eter affects precision of the weighted periodogram operator estimator, and the impact of the magnitude of parameter T is quite strong. This fact can be observed looking at differences in the magnitude of empirical mean quadratic errors, based on 100 repetitions, associated with the weighted periodogram operator for $T = 50$ and $T = 100$, considering bandwidth parameter $B_T = 0.1$, as well as for $T = 500$, and $T = 1000$, considering bandwidth parameter $B_T = 0.2$, since a substantial reduction in such magnitudes occurs when increasing the functional sample size T (see, e.g., Theorem 3.6 in Panaretos and Tavakoli, 2013). The empirical distribution of the temporal mean of the empirical absolute errors (T.M.E.A.E.s) associated with the minimum contrast parameter estimator of the elements of the spectral density operator family near the zero frequency is also displayed from projection into H_n, $n = 1, \ldots, 15$ (right–hand side of Figures 35–38).

(a) $T = 50, R = 100$

(b) $T = 50, R = 2000$

(c) $T = 50, R = 5000$

(d) $T = 500, R = 100$

(e) $T = 500, R = 2000$

(f) $T = 500, R = 5000$

(g) $T = 1000, R = 100$

(h) $T = 1000, R = 2000$

(i) $T = 1000, R = 5000$

Fig. 13: Empirical probabilities (4.13) (LRD operator nondecreasing eigenvalues, multifractionally integrated SPHAR(1) process)

(a) $R = 100$, scales 1–5 (b) $R = 2000$, scales 1–5 (c) $R = 5000$, scales 1–5

(d) $R = 100$, scales 10–15 (e) $R = 2000$, scales 10–15 (f) $R = 5000$, scales 10–15

(g) $R = 100$, scales 20–25 (h) $R = 2000$, scales 20–25 (i) $R = 5000$, scales 20–25

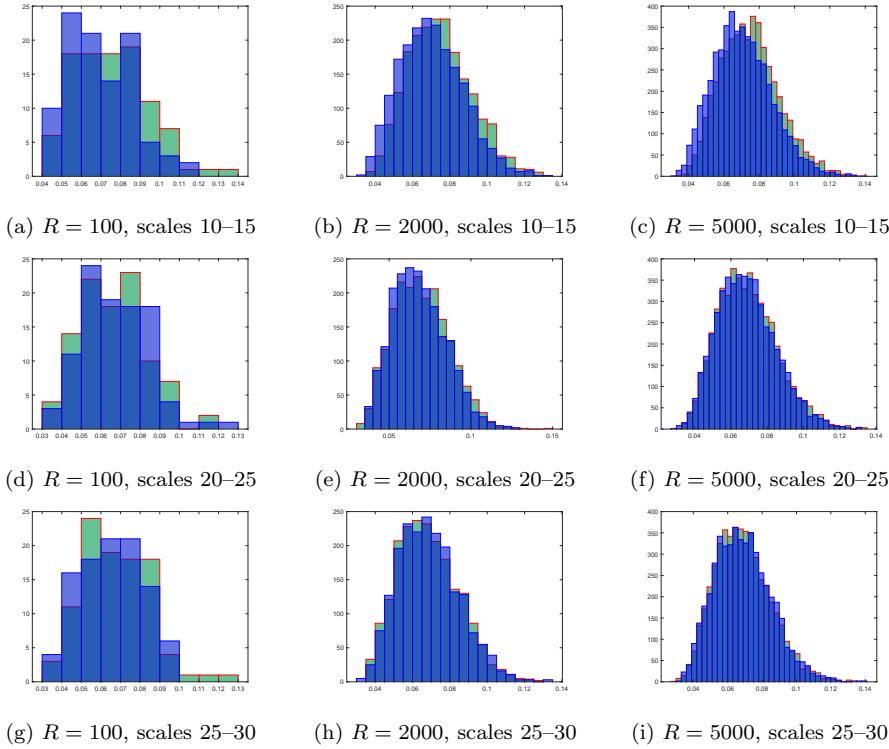(j) $R = 100$, scales 25–30 (k) $R = 2000$, scales 25–30 (l) $R = 5000$, scales 25–30

Fig. 14: Histograms of the temporal mean of the empirical absolute errors, for the sample size $T = 50$ (LRD operator decreasing eigenvalues, multifractionally integrated SPHAR(3) process)

(a) $R = 100$, scales 1–5   (b) $R = 2000$, scales 1–5   (c) $R = 5000$, scales 1–5

(d) $R = 100$, scales 10–15   (e) $R = 2000$, scales 10–15   (f) $R = 5000$, scales 10–15

(g) $R = 100$, scales 20–25   (h) $R = 2000$, scales 20–25   (i) $R = 5000$, scales 20–25

(j) $R = 100$, scales 25–30   (k) $R = 2000$, scales 25–30   (l) $R = 5000$, scales 25–30

Fig. 15: Histograms of the temporal mean of the empirical absolute errors, for the sample size $T = 500$ (LRD operator decreasing eigenvalues, multifractionally integrated SPHAR(3) process)

(a) $R = 100$, scales 1–5   (b) $R = 2000$, scales 1–5   (c) $R = 5000$, scales 1–5

(d) $R = 100$, scales 10–15   (e) $R = 2000$, scales 10–15   (f) $R = 5000$, scales 10–15

(g) $R = 100$, scales 20–25   (h) $R = 2000$, scales 20–25   (i) $R = 5000$, scales 20–25

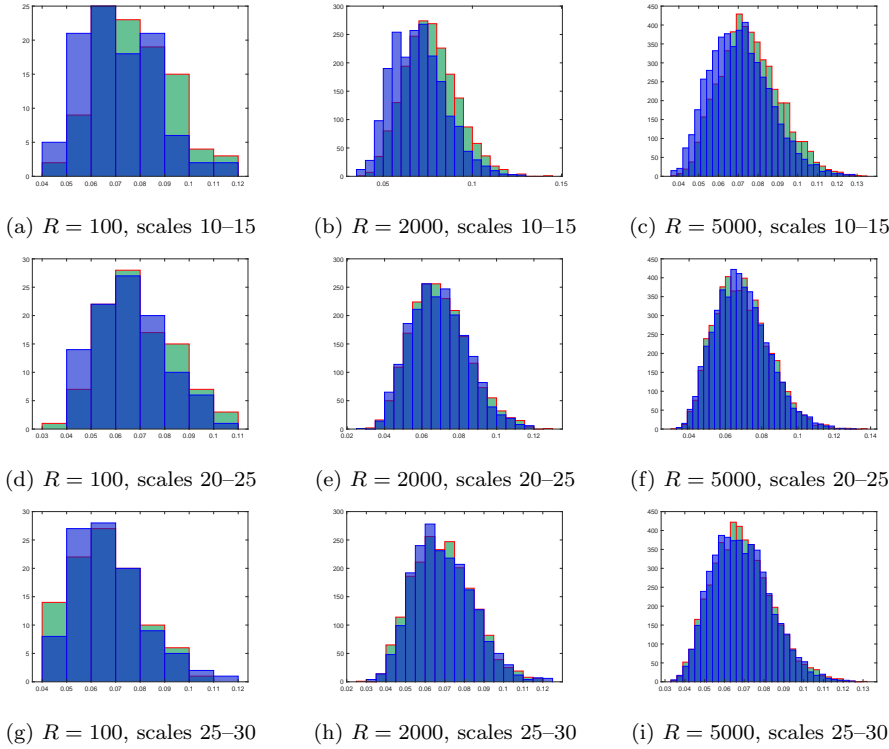(j) $R = 100$, scales 25–30   (k) $R = 2000$, scales 25–30   (l) $R = 5000$, scales 25–30

Fig. 16: Histograms of the temporal mean of the empirical absolute errors, for the sample size $T = 50$ (LRD operator nondecreasing eigenvalues, multifractionally integrated SPHAR(3) process)

(a) $R = 100$, scales 10–15   (b) $R = 2000$, scales 10–15   (c) $R = 5000$, scales 10–15

(d) $R = 100$, scales 20–25   (e) $R = 2000$, scales 20–25   (f) $R = 5000$, scales 20–25

(g) $R = 100$, scales 25–30   (h) $R = 2000$, scales 25–30   (i) $R = 5000$, scales 25–30

Fig. 17: Histograms of the temporal mean of the empirical absolute errors, for the sample size $T = 500$ (LRD operator nondecreasing eigenvalues, multifractionally integrated SPHAR(3) process)

(a) $R = 100$, scales 10–15 (b) $R = 2000$, scales 10–15 (c) $R = 5000$, scales 10–15

(d) $R = 100$, scales 20–25 (e) $R = 2000$, scales 20–25 (f) $R = 5000$, scales 20–25

(g) $R = 100$, scales 25–30 (h) $R = 2000$, scales 25–30 (i) $R = 5000$, scales 25–30

Fig. 18: Histograms of the temporal mean of the empirical absolute errors, for the sample size $T = 1000$ (LRD operator nondecreasing eigenvalues, multi-fractionally integrated SPHAR(3) process)

(a) $R = 100$, scales 1–5

(b) $R = 2000$, scales 1–5

(c) $R = 5000$, scales 1–5

(d) $R = 100$, scales 10–15

(e) $R = 2000$, scales 10–15

(f) $R = 5000$, scales 10–15

(g) $R = 100$, scales 20–25

(h) $R = 2000$, scales 20–25

(i) $R = 5000$, scales 20–25

(j) $R = 100$, scales 25–30

(k) $R = 2000$, scales 25–30

(l) $R = 5000$, scales 25–30

Fig. 19: Histograms of the temporal mean of the empirical absolute errors, for the sample size $T = 50$ (LRD operator decreasing eigenvalues, multifractionally integrated SPHARMA(1,1) process)

(a) $R = 100$, scales 1–5 (b) $R = 2000$, scales 1–5 (c) $R = 5000$, scales 1–5

(d) $R = 100$, scales 10–15 (e) $R = 2000$, scales 10–15 (f) $R = 5000$, scales 10–15

(g) $R = 100$, scales 20–25 (h) $R = 2000$, scales 20–25 (i) $R = 5000$, scales 20–25

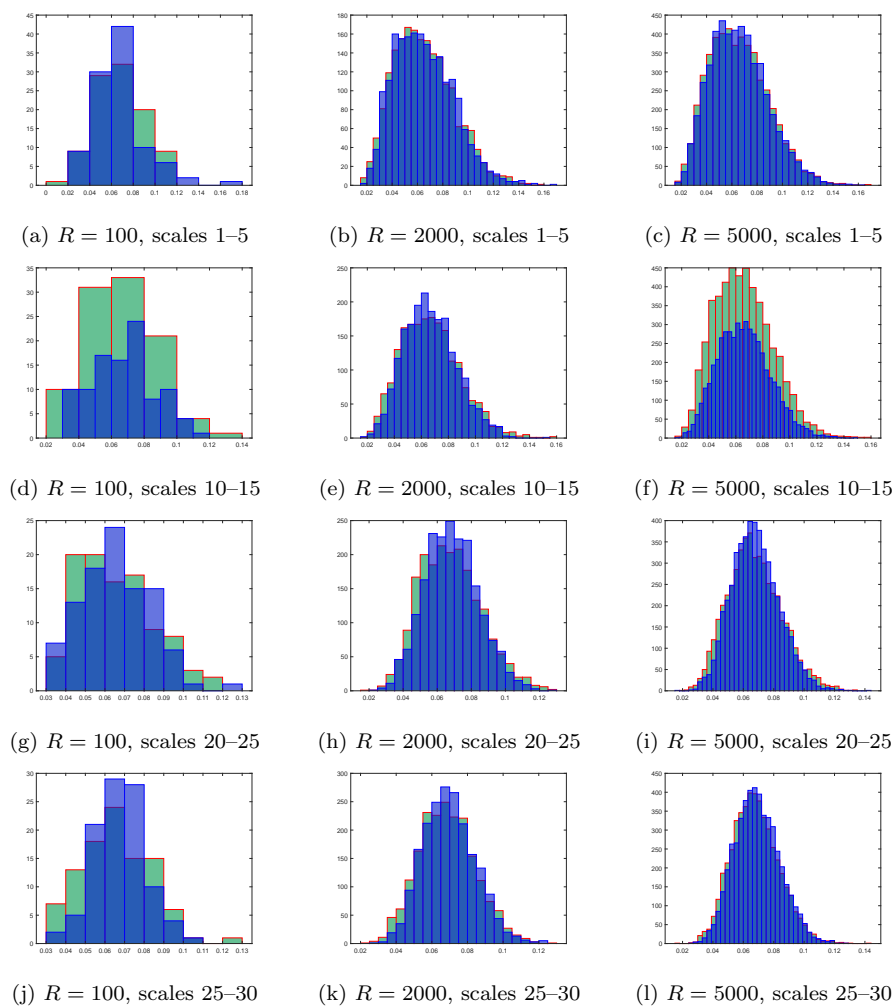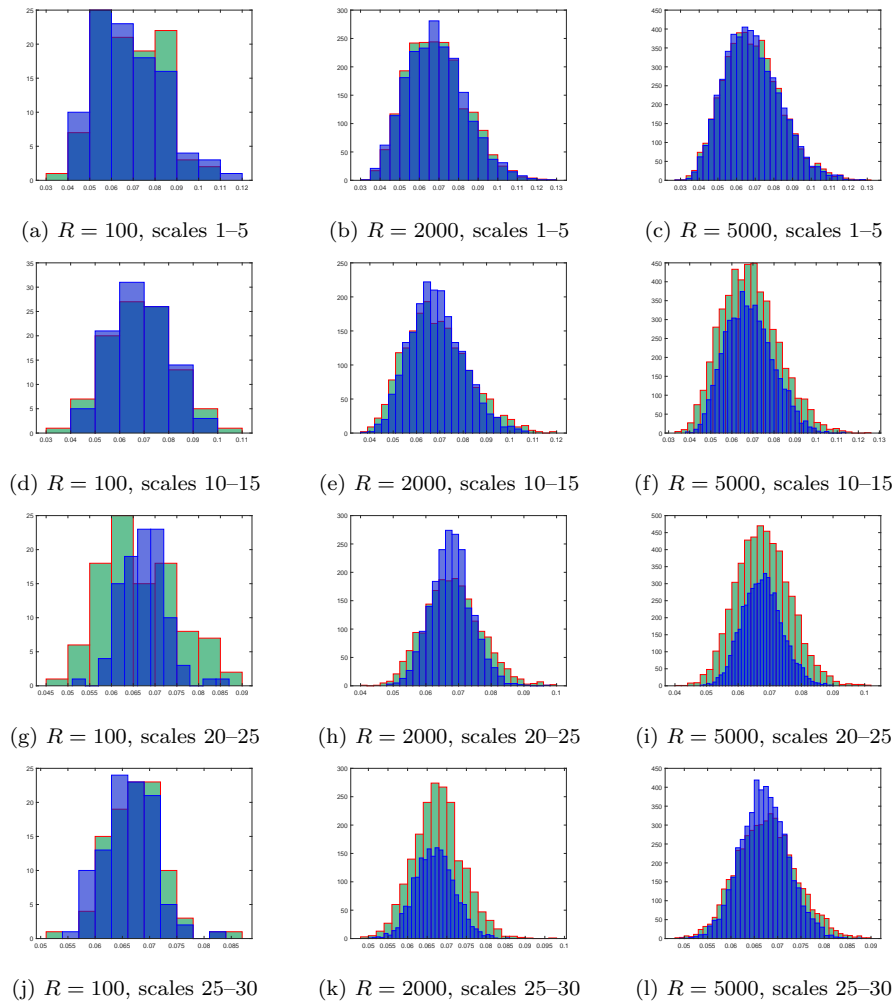(j) $R = 100$, scales 25–30 (k) $R = 2000$, scales 25–30 (l) $R = 5000$, scales 25–30

Fig. 20: Histograms of the temporal mean of the empirical absolute errors, for the sample size $T = 500$ (LRD operator decreasing eigenvalues, multifractionally integrated SPHARMA(1,1) process)

(a) $R = 100$, scales 1–5   (b) $R = 2000$, scales 1–5   (c) $R = 5000$, scales 1–5

(d) $R = 100$, scales 10–15   (e) $R = 2000$, scales 10–15   (f) $R = 5000$, scales 10–15

(g) $R = 100$, scales 20–25   (h) $R = 2000$, scales 20–25   (i) $R = 5000$, scales 20–25

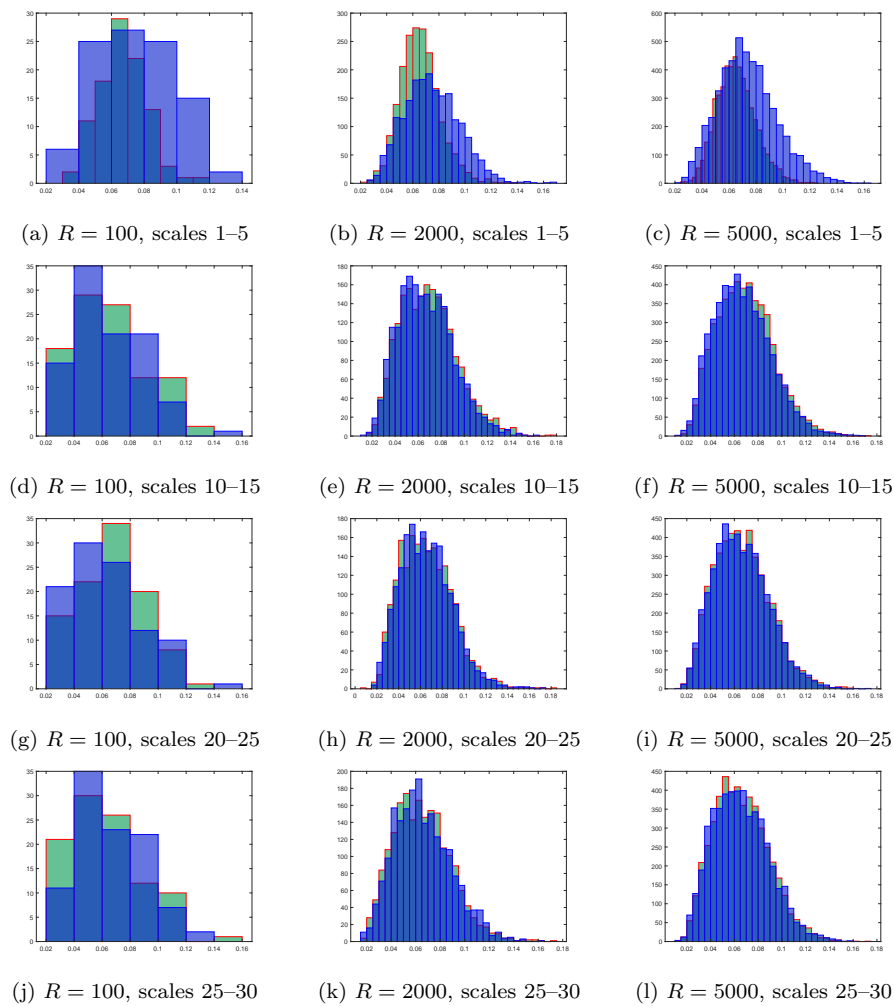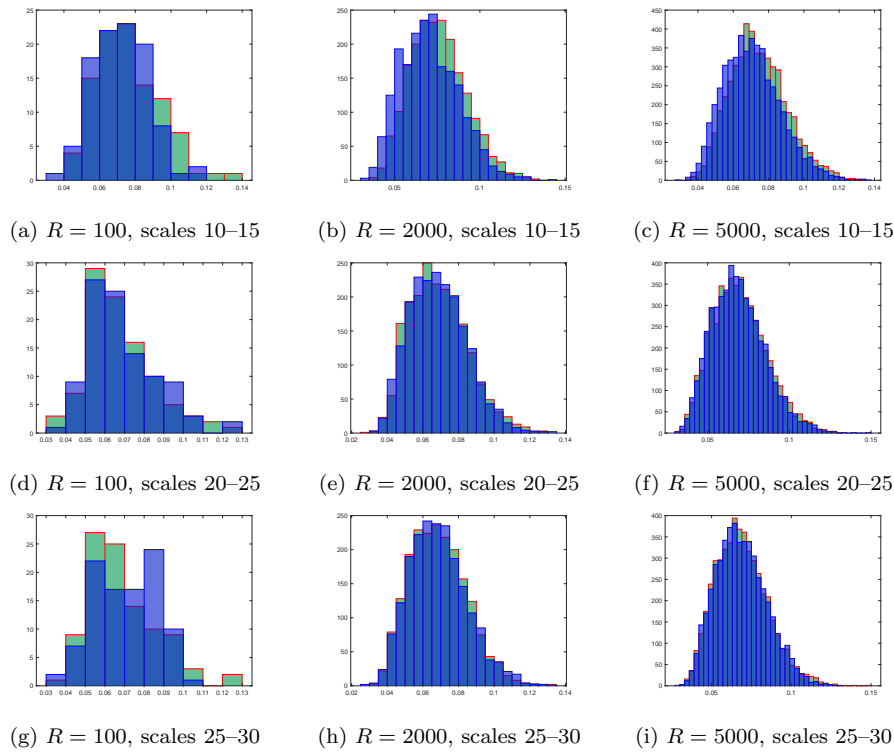(j) $R = 100$, scales 25–30   (k) $R = 2000$, scales 25–30   (l) $R = 5000$, scales 25–30

Fig. 21: Histograms of the temporal mean of the empirical absolute errors, for the sample size $T = 1000$ (LRD operator decreasing eigenvalues, multifractionally integrated SPHARMA(1,1) process)

(a) $T = 50, R = 100$ (b) $T = 50, R = 2000$ (c) $T = 50, R = 5000$

(d) $T = 500, R = 100$ (e) $T = 500, R = 2000$ (f) $T = 500, R = 5000$

(g) $T = 1000, R = 100$ (h) $T = 1000, R = 2000$ (i) $T = 1000, R = 5000$

Fig. 22: Empirical probabilities (4.13) (LRD operator decreasing eigenvalues, multifractionally integrated SPHARMA(1,1) process)

(a) $R = 100$, scales 10–15   (b) $R = 2000$, scales 10–15   (c) $R = 5000$, scales 10–15

(d) $R = 100$, scales 20–25   (e) $R = 2000$, scales 20–25   (f) $R = 5000$, scales 20–25

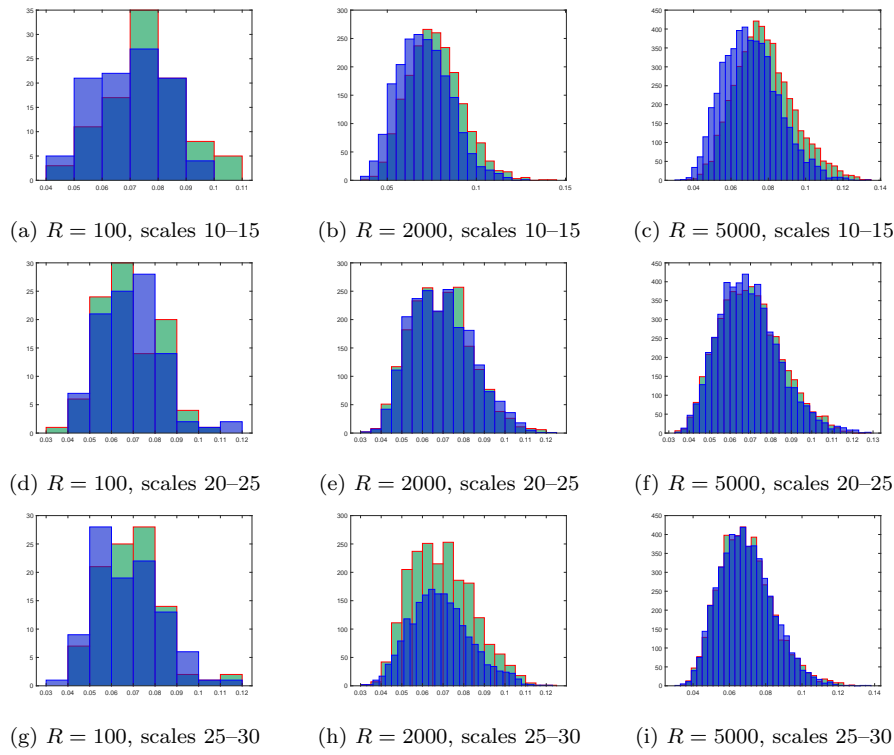(g) $R = 100$, scales 25–30   (h) $R = 2000$, scales 25–30   (i) $R = 5000$, scales 25–30

Fig. 23: Histograms of the temporal mean of the empirical absolute errors, for the sample size $T = 50$ (LRD operator nondecreasing eigenvalues, multifractionally integrated SPHARMA(1,1) process)

(a) $R = 100$, scales 10–15   (b) $R = 2000$, scales 10–15   (c) $R = 5000$, scales 10–15

(d) $R = 100$, scales 20–25   (e) $R = 2000$, scales 20–25   (f) $R = 5000$, scales 20–25

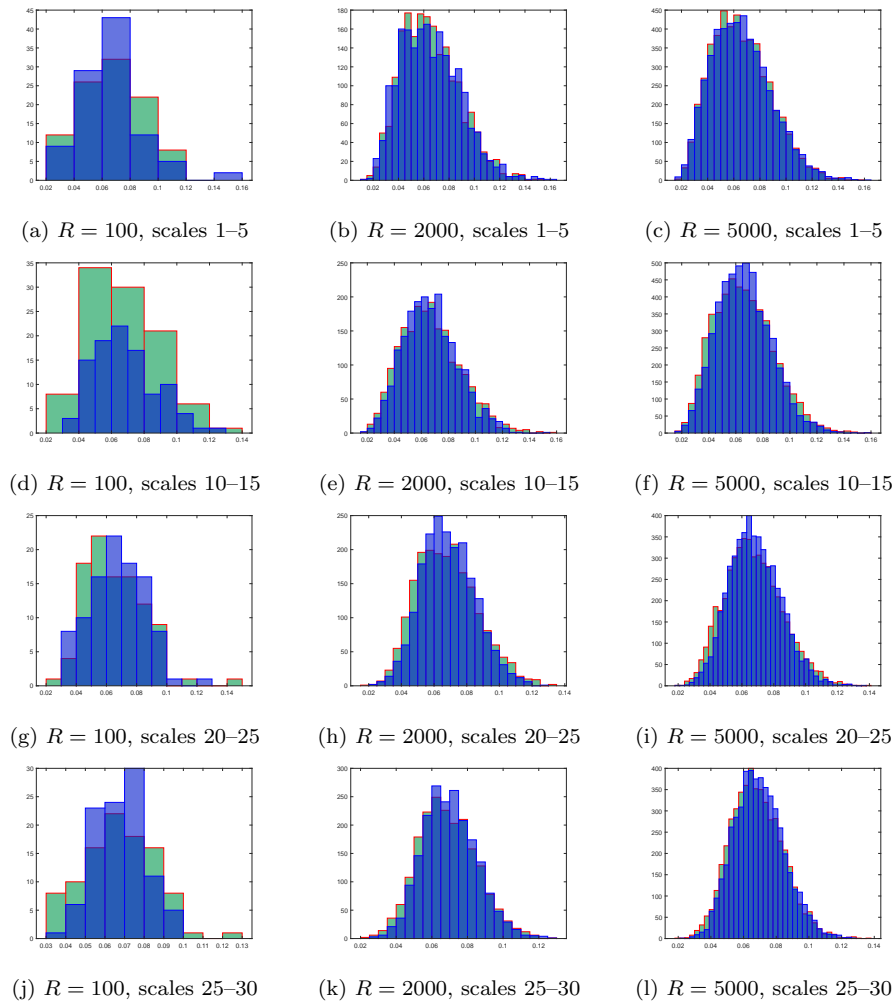(g) $R = 100$, scales 25–30   (h) $R = 2000$, scales 25–30   (i) $R = 5000$, scales 25–30

Fig. 24: Histograms of the temporal mean of the empirical absolute errors, for the sample size $T = 500$ (LRD operator nondecreasing eigenvalues, multifractionally integrated SPHARMA(1,1) process)

(a) $R = 100$, scales 10–15 (b) $R = 2000$, scales 10–15 (c) $R = 5000$, scales 10–15

(d) $R = 100$, scales 20–25 (e) $R = 2000$, scales 20–25 (f) $R = 5000$, scales 20–25

(g) $R = 100$, scales 25–30 (h) $R = 2000$, scales 25–30 (i) $R = 5000$, scales 25–30
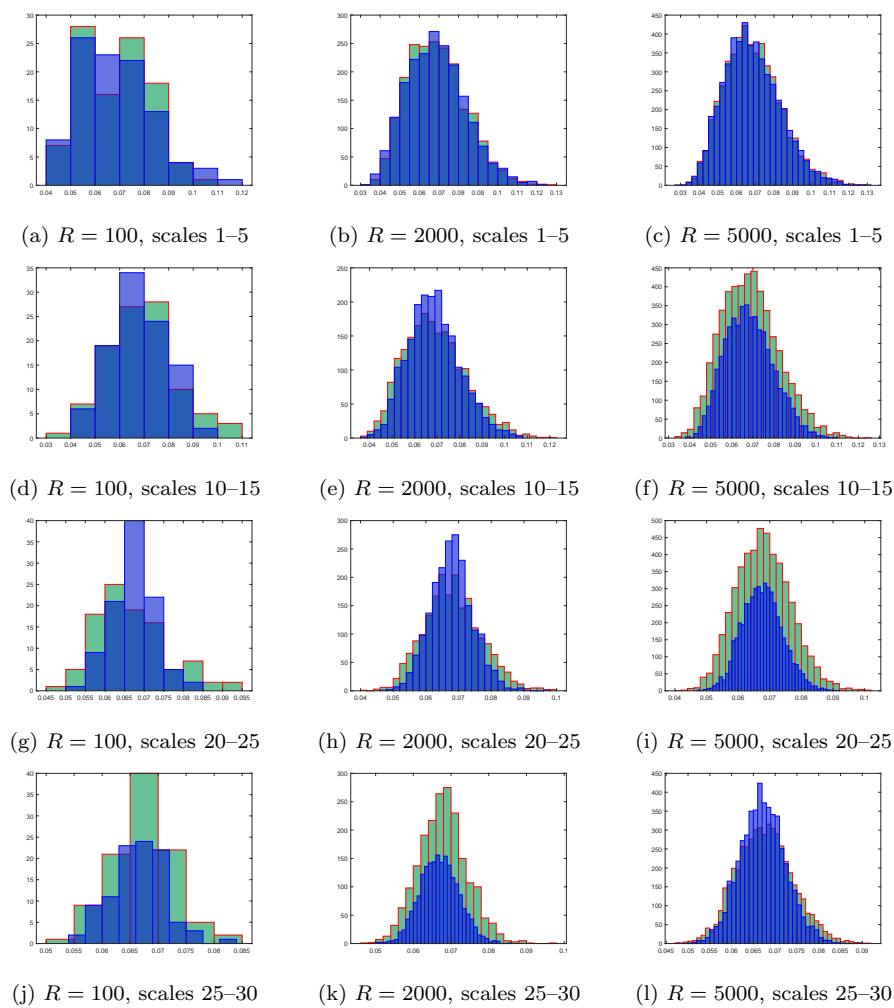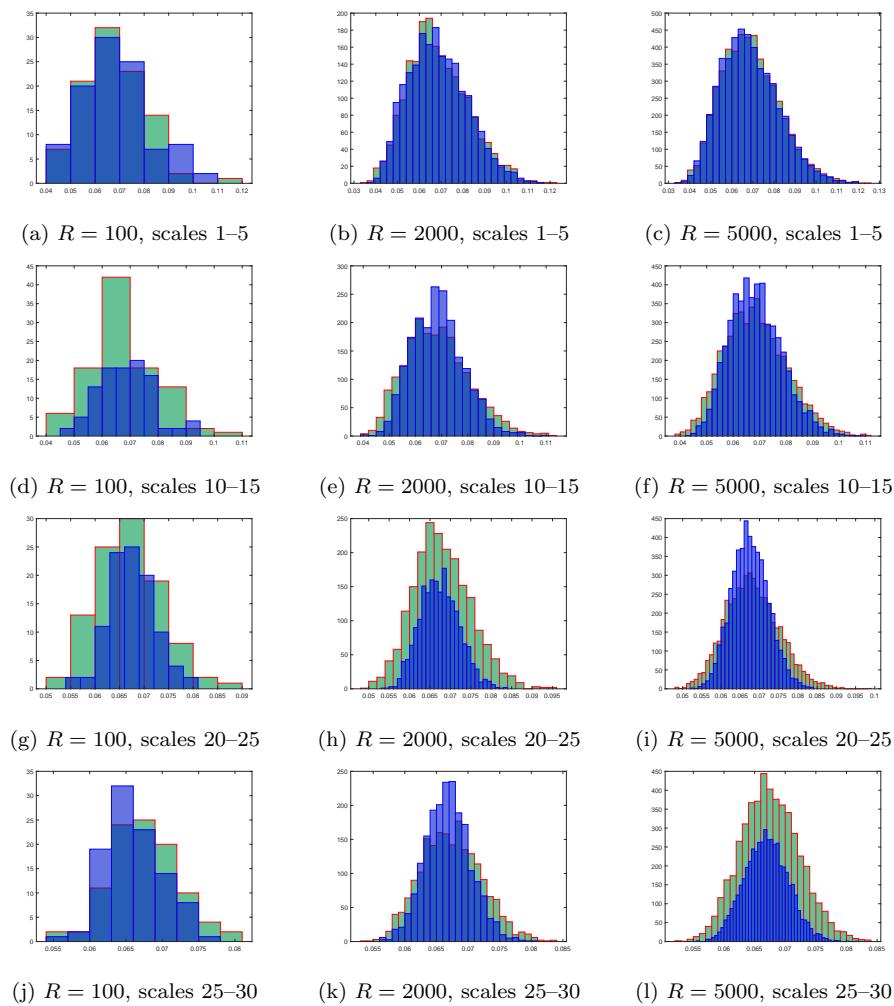
Fig. 25: Histograms of the temporal mean of the empirical absolute errors, for the sample size $T = 1000$ (LRD operator nondecreasing eigenvalues, multifractionally integrated SPHARMA(1,1) process)

(a) $T = 50, R = 100$

(b) $T = 50, R = 2000$

(c) $T = 50, R = 5000$

(d) $T = 500, R = 100$

(e) $T = 500, R = 2000$

(f) $T = 500, R = 5000$

(g) $T = 1000, R = 100$

(h) $T = 1000, R = 2000$

(i) $T = 1000, R = 5000$

Fig. 26: Empirical probabilities (4.13) (LRD operator nondecreasing eigenvalues, multifractionally integrated SPHARMA(1,1) process)

(a) $R = 100$, scales 1–5   (b) $R = 2000$, scales 1–5   (c) $R = 5000$, scales 1–5

(d) $R = 100$, scales 10–15   (e) $R = 2000$, scales 10–15   (f) $R = 5000$, scales 10–15

(g) $R = 100$, scales 20–25   (h) $R = 2000$, scales 20–25   (i) $R = 5000$, scales 20–25

(j) $R = 100$, scales 25–30   (k) $R = 2000$, scales 25–30   (l) $R = 5000$, scales 25–30

Fig. 27: Histograms of the temporal mean of the empirical absolute errors, for the sample size $T = 50$ (LRD operator decreasing eigenvalues, multifractionally integrated SPHARMA(3,1) process)
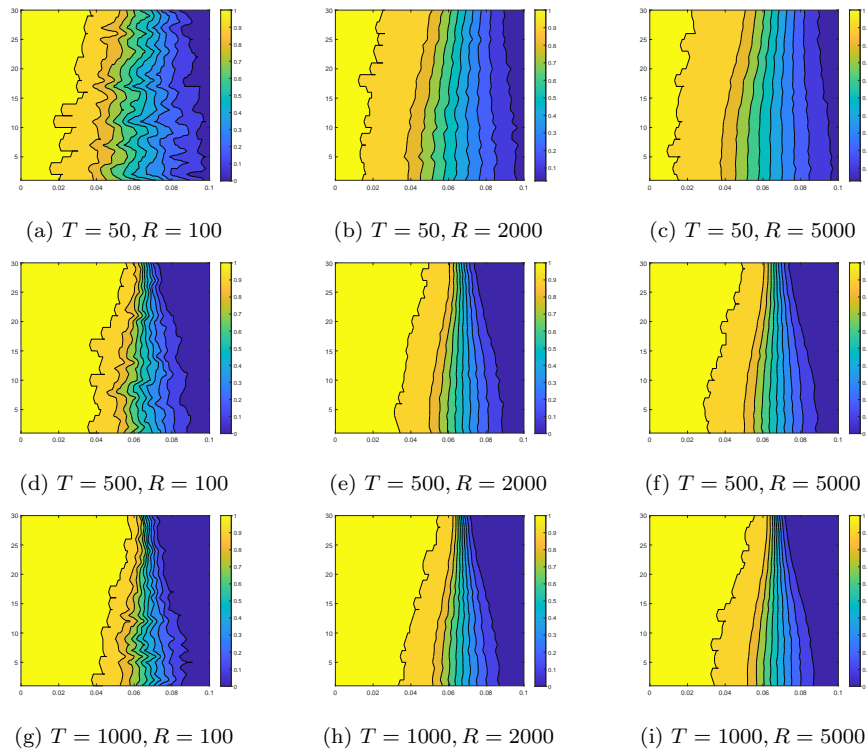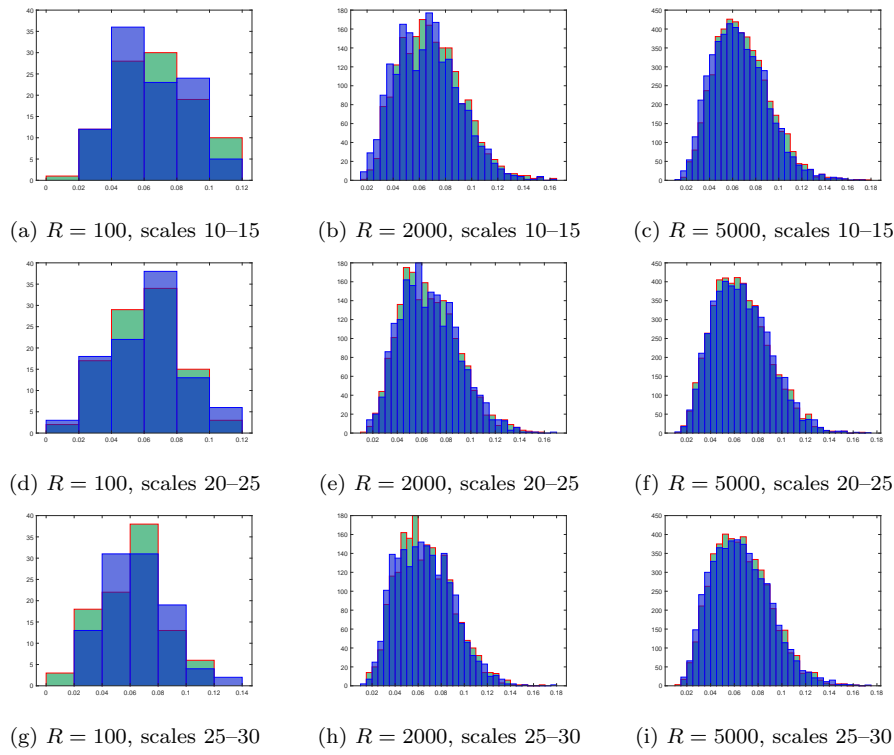
(a) $R = 100$, scales 1–5   (b) $R = 2000$, scales 1–5   (c) $R = 5000$, scales 1–5

(d) $R = 100$, scales 10–15   (e) $R = 2000$, scales 10–15   (f) $R = 5000$, scales 10–15

(g) $R = 100$, scales 20–25   (h) $R = 2000$, scales 20–25   (i) $R = 5000$, scales 20–25

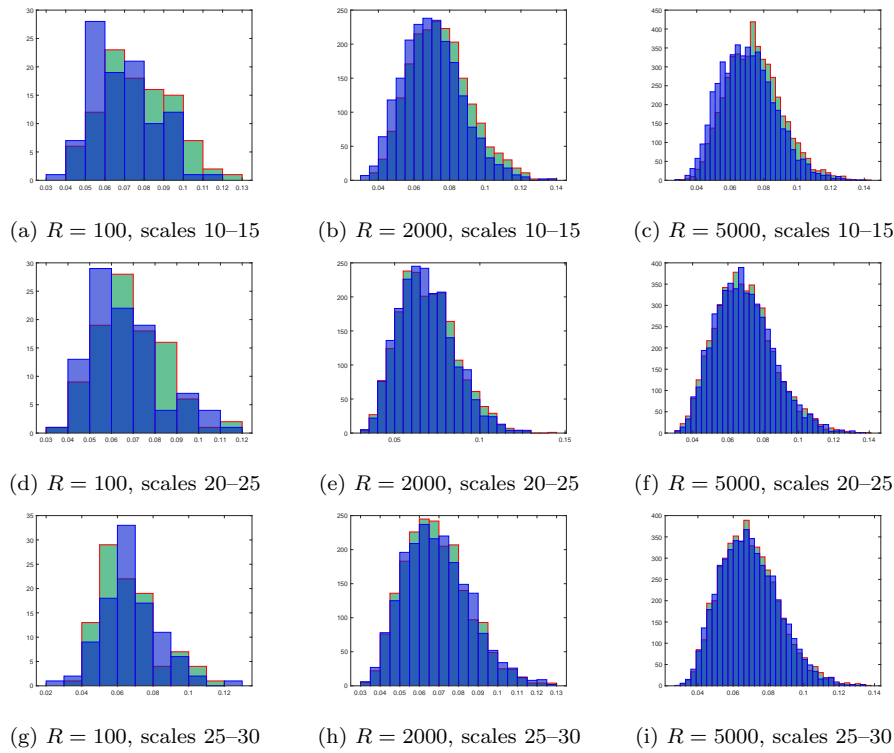(j) $R = 100$, scales 25–30   (k) $R = 2000$, scales 25–30   (l) $R = 5000$, scales 25–30

Fig. 28: Histograms of the temporal mean of the empirical absolute errors, for the sample size $T = 500$ (LRD operator decreasing eigenvalues, multifractionally integrated SPHARMA(3,1) process)

(a) $R = 100$, scales 1–5 (b) $R = 2000$, scales 1–5 (c) $R = 5000$, scales 1–5

(d) $R = 100$, scales 10–15 (e) $R = 2000$, scales 10–15 (f) $R = 5000$, scales 10–15

(g) $R = 100$, scales 20–25 (h) $R = 2000$, scales 20–25 (i) $R = 5000$, scales 20–25

(j) $R = 100$, scales 25–30 (k) $R = 2000$, scales 25–30 (l) $R = 5000$, scales 25–30

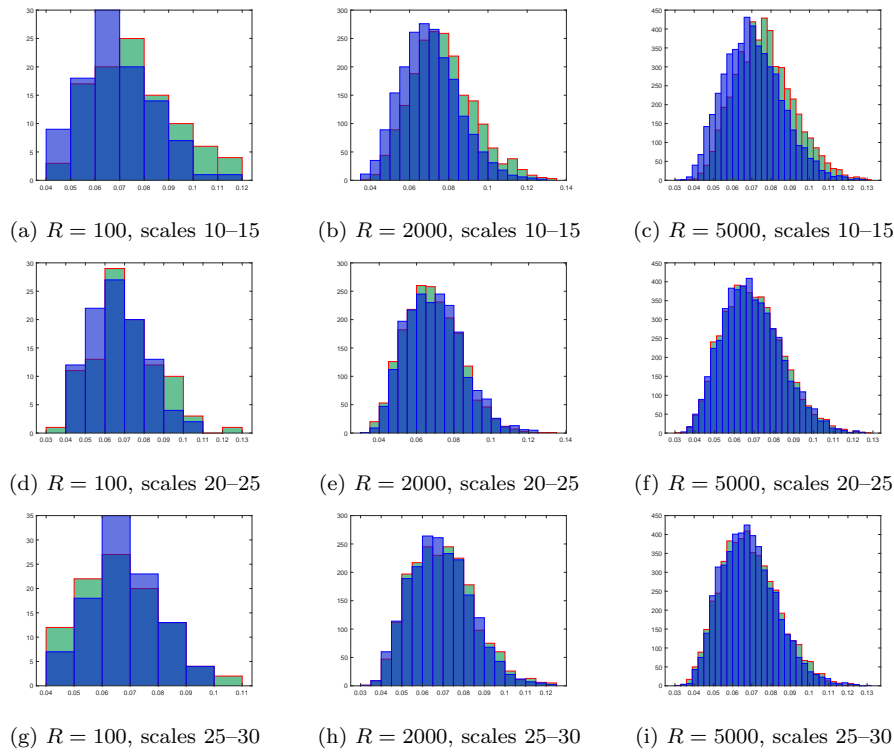Fig. 29: Histograms of the temporal mean of the empirical absolute errors, for the sample size $T = 1000$ (LRD operator decreasing eigenvalues, multifractionally integrated SPHARMA(3,1) process)
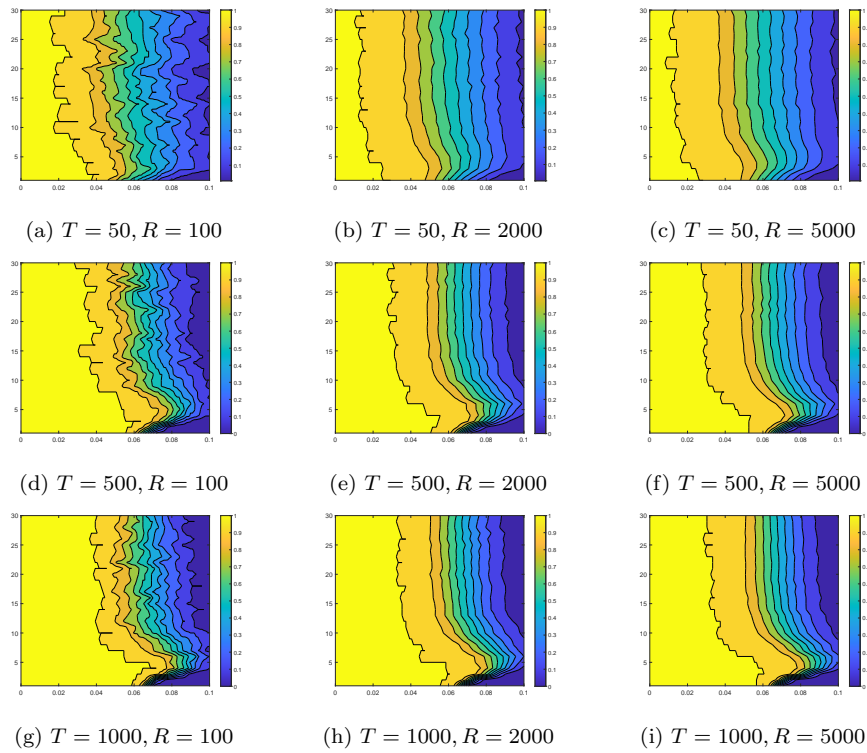
(a) $T = 50, R = 100$ (b) $T = 50, R = 2000$ (c) $T = 50, R = 5000$

(d) $T = 500, R = 100$ (e) $T = 500, R = 2000$ (f) $T = 500, R = 5000$

(g) $T = 1000, R = 100$ (h) $T = 1000, R = 2000$ (i) $T = 1000, R = 5000$

Fig. 30: Empirical probabilities (4.13) (LRD operator decreasing eigenvalues, multifractionally integrated SPHARMA(3,1) process)

(a) $R = 100$, scales 10–15

(b) $R = 2000$, scales 10–15

(c) $R = 5000$, scales 10–15

(d) $R = 100$, scales 20–25

(e) $R = 2000$, scales 20–25

(f) $R = 5000$, scales 20–25

(g) $R = 100$, scales 25–30

(h) $R = 2000$, scales 25–30
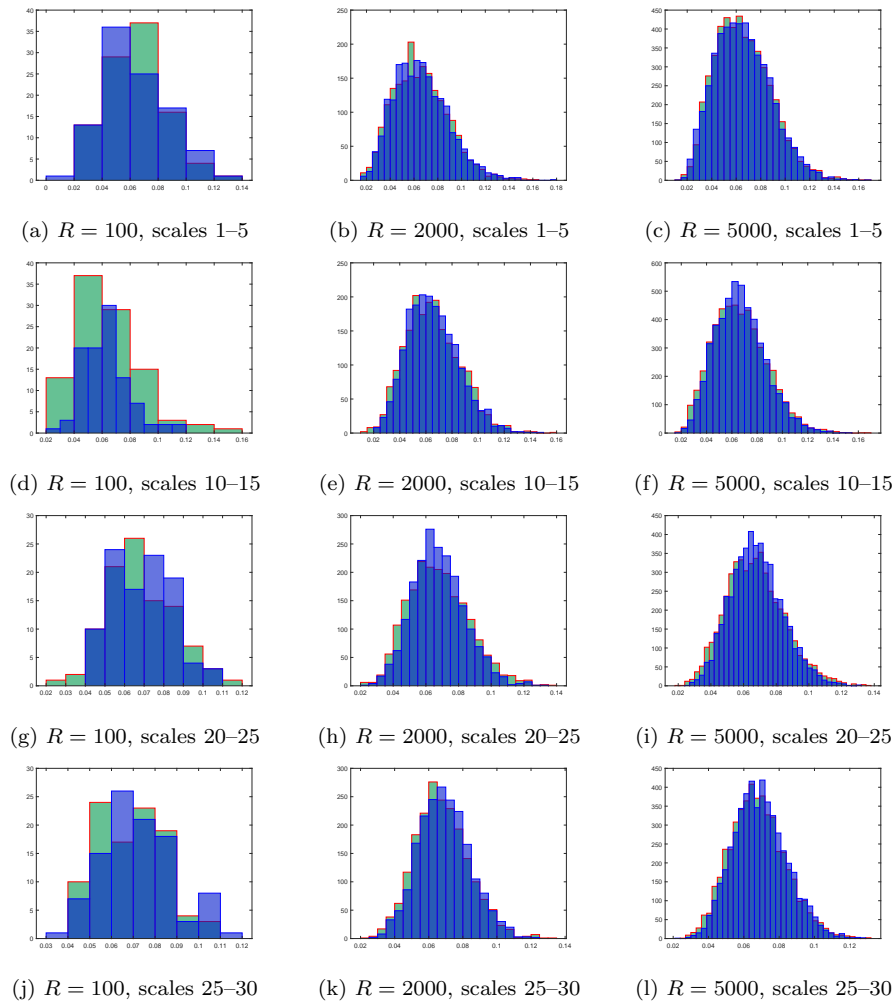
(i) $R = 5000$, scales 25–30

Fig. 31: Histograms of the temporal mean of the empirical absolute errors, for the sample size $T = 50$ (LRD operator nondecreasing eigenvalues, multifractionally integrated SPHARMA(3,1) process)
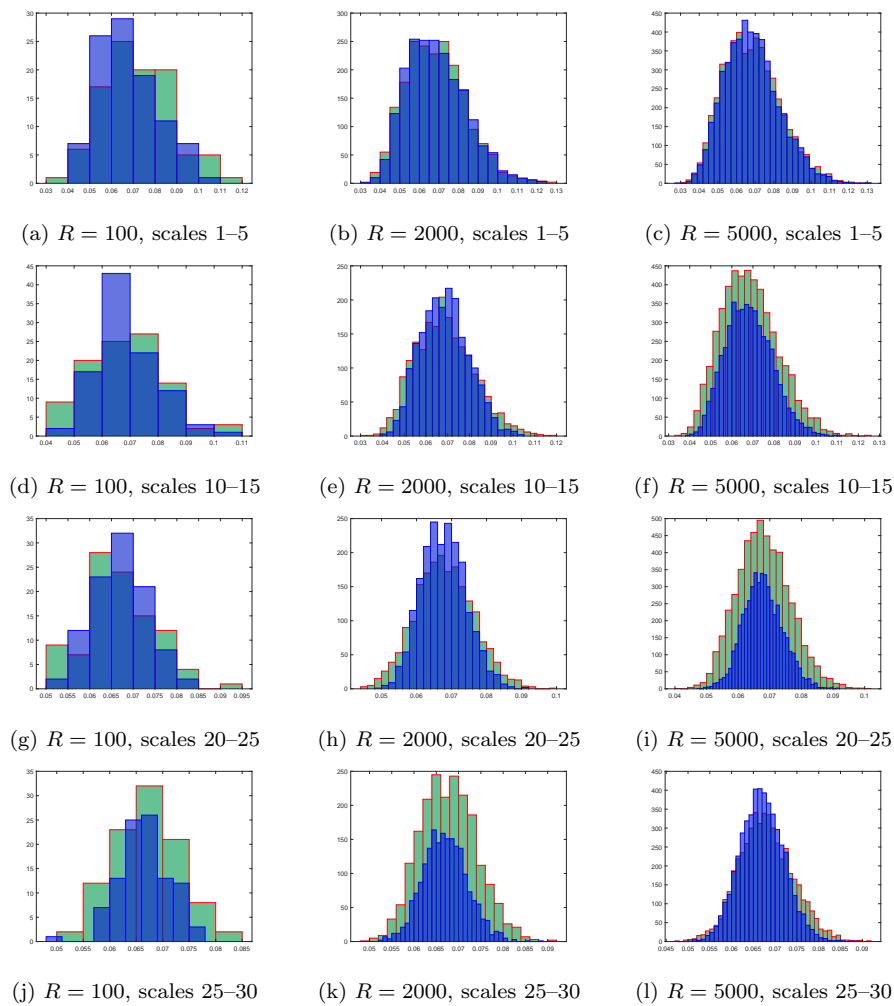
(a) $R = 100$, scales 10–15   (b) $R = 2000$, scales 10–15   (c) $R = 5000$, scales 10–15

(d) $R = 100$, scales 20–25   (e) $R = 2000$, scales 20–25   (f) $R = 5000$, scales 20–25

(g) $R = 100$, scales 25–30   (h) $R = 2000$, scales 25–30   (i) $R = 5000$, scales 25–30

Fig. 32: Histograms of the temporal mean of the empirical absolute errors, for the sample size $T = 500$ (LRD operator nondecreasing eigenvalues, multifractionally integrated SPHARMA(3,1) process)
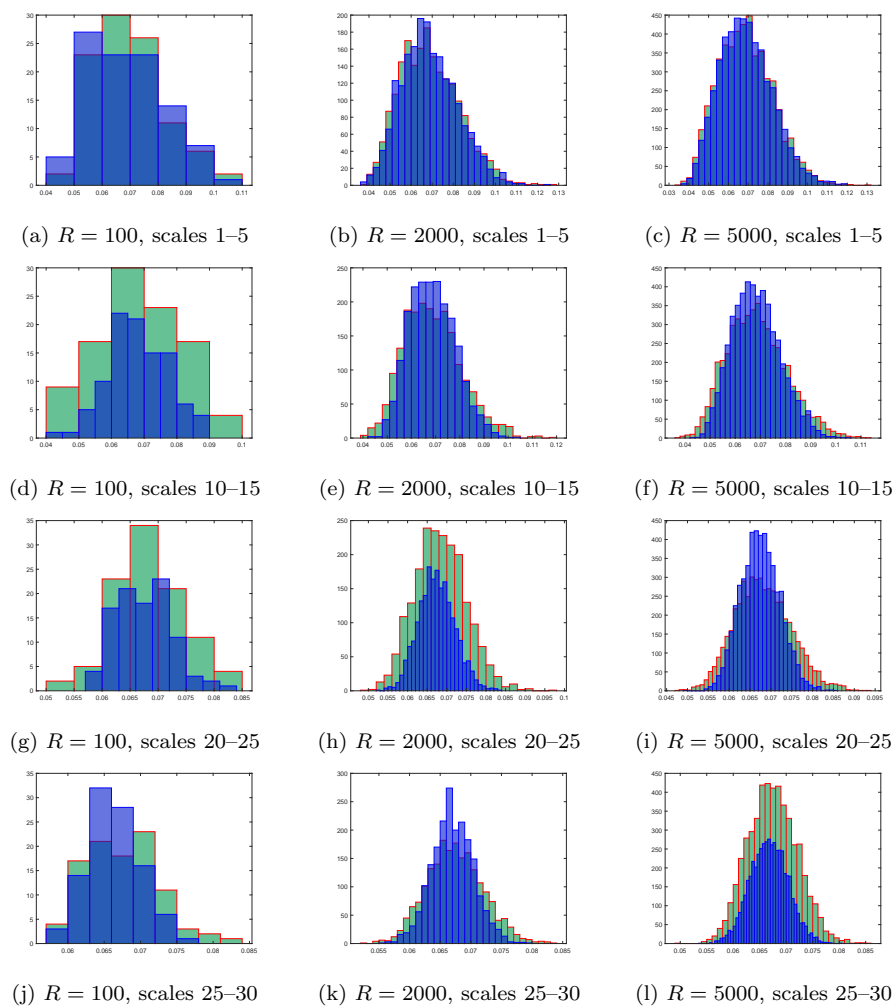
(a) $R = 100$, scales 10–15

(b) $R = 2000$, scales 10–15

(c) $R = 5000$, scales 10–15

(d) $R = 100$, scales 20–25

(e) $R = 2000$, scales 20–25

(f) $R = 5000$, scales 20–25

(g) $R = 100$, scales 25–30

(h) $R = 2000$, scales 25–30

(i) $R = 5000$, scales 25–30

Fig. 33: Histograms of the temporal mean of the empirical absolute errors, for the sample size $T = 1000$ (LRD operator nondecreasing eigenvalues, multifractionally integrated SPHARMA(3,1) process)
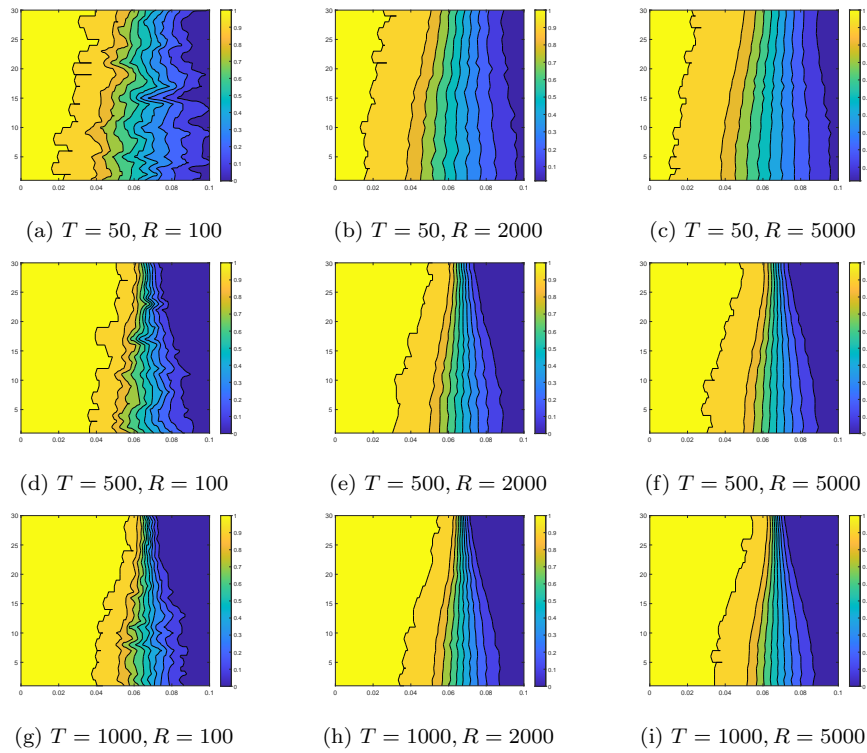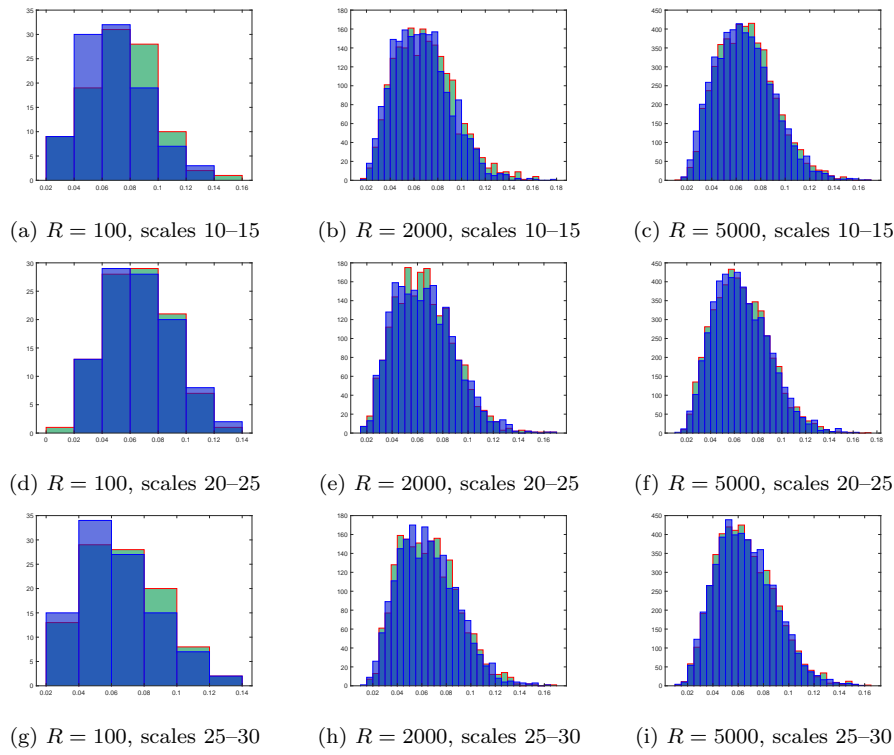
(a) $T = 50, R = 100$

(b) $T = 50, R = 2000$

(c) $T = 50, R = 5000$

(d) $T = 500, R = 100$

(e) $T = 500, R = 2000$

(f) $T = 500, R = 5000$

(g) $T = 1000, R = 100$

(h) $T = 1000, R = 2000$

(i) $T = 1000, R = 5000$

Fig. 34: Empirical probabilities (4.13) (LRD operator nondecreasing eigenvalues, multifractionally integrated SPHARMA(3,1) process)

(a) SPHAR(1). E.M.Q.E. of P.W.P.O.
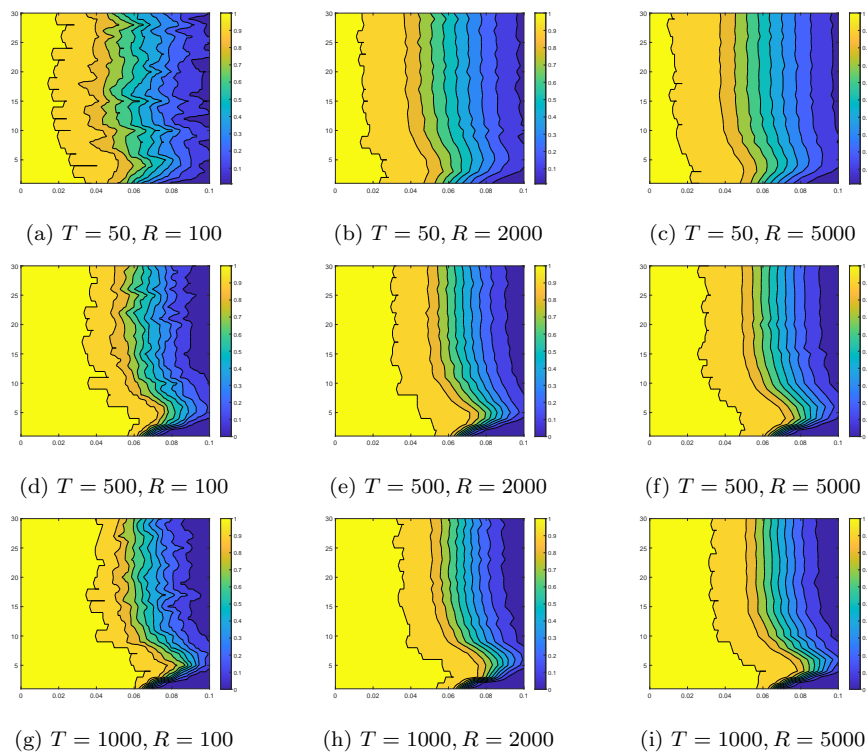
(b) M.I. SPHAR(1). Scales 1 − 5. T.M.E.A.E. histograms

(c) M.I. SPHAR(1). Scales 10 − 15. T.M.E.A.E. histograms

(d) SPHAR(3). E.M.Q.E. of P.W.P.O.

(e) M.I. SPHAR(3). Scales 1 − 5. T.M.E.A.E. histograms

(f) M.I. SPHAR(3). Scales 10 − 15. T.M.E.A.E. histograms

(g) SPHARMA(1,1). E.M.Q.E. of P.W.P.O.

(h) M.I. SPHARMA(1,1). Scales 1 − 5. T.M.E.A.E. histograms

(i) M.I. SPHARMA(1,1). Scales 10 − 15. T.M.E.A.E. histograms

(j) SPHARMA(3,1). E.M.Q.E. of P.W.P.O.

(k) M.I. SPHARMA(3,1). Scales 1 − 5. T.M.E.A.E. histograms

(l) M.I. SPHARMA(3,1). Scales 10 − 15. T.M.E.A.E. histograms

Fig. 35: For the four families of multifractionally integrated functional spherical processes, the empirical mean quadratic errors associated with the weighted periodogram operator estimator, from projection into the eigenspaces H_n, $n = 16, \ldots, 30$, of the spherical Laplace Beltrami operator, are displayed (left–hand side). The bandwidth parameter $B_T = 0.1$ is chosen in all the cases. The remaining plots provide the histograms of the temporal mean of the empirical absolute errors, associated with the minimum contrast parameter estimation, from projection into the eigenspaces H_n, $n = 1, 5, 10, 15$, of the spherical Laplace Beltrami operator based on a functional sample size $T = 50$, and $R = 100$ repetitions

(a) SPHAR(1). E.M.Q.E. of P.W.P.O.

(b) M.I. SPHAR(1). Scales 1 − 5. T.M.E.A.E. histograms

(c) M.I. SPHAR(1). Scales 10 − 15. T.M.E.A.E. histograms

(d) SPHAR(3). E.M.Q.E. of P.W.P.O.

(e) M.I. SPHAR(3). Scales 1 − 5. T.M.E.A.E. histograms

(f) M.I. SPHAR(3). Scales 10 − 15. T.M.E.A.E. histograms

(g)   SPHARMA(1,1). E.M.Q.E. of P.W.P.O.

(h) M.I. SPHARMA(1,1). Scales 1 − 5. T.M.E.A.E. histograms

(i) M.I. SPHARMA(1,1). Scales 10 − 15. T.M.E.A.E. histograms

(j)   SPHARMA(3,1). E.M.Q.E. of P.W.P.O.

(k) M.I. SPHARMA(3,1). Scales 1 − 5. T.M.E.A.E. histograms

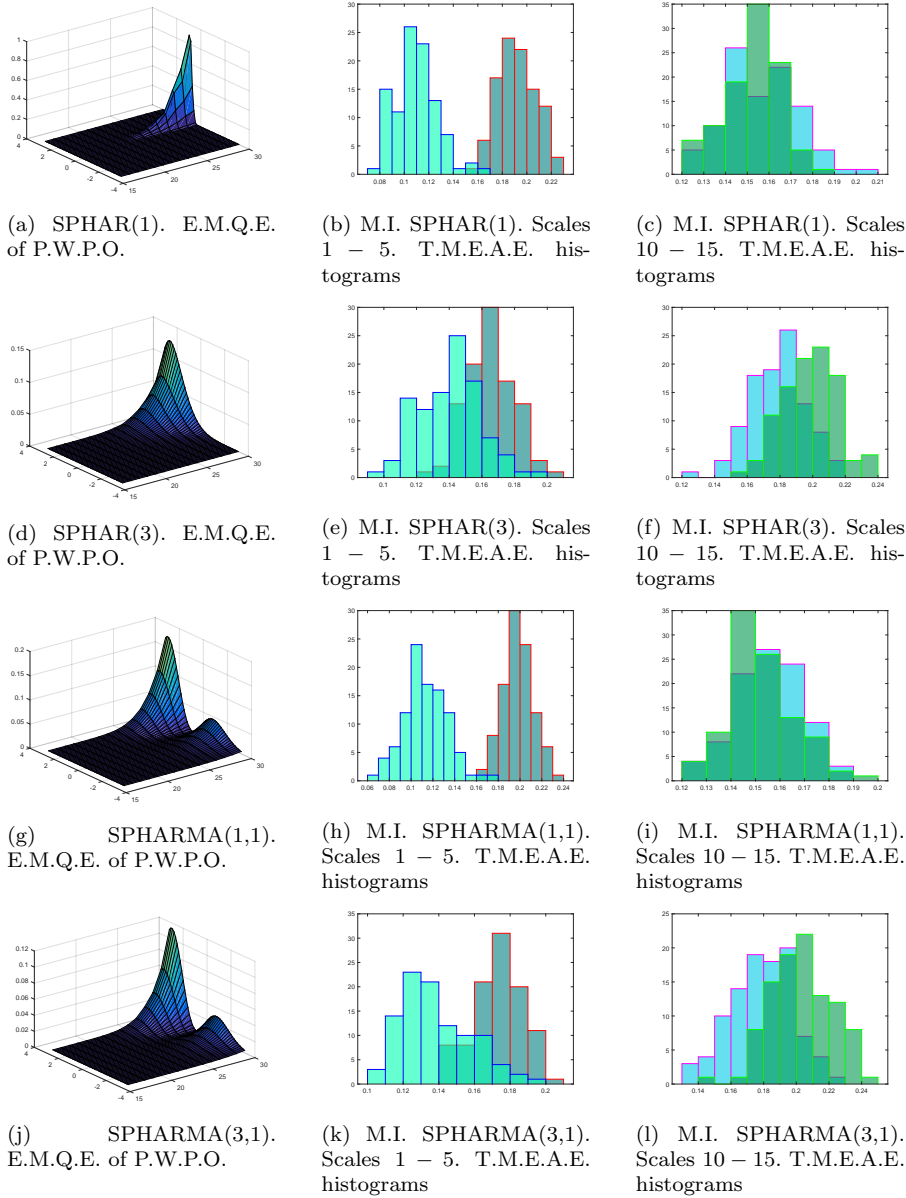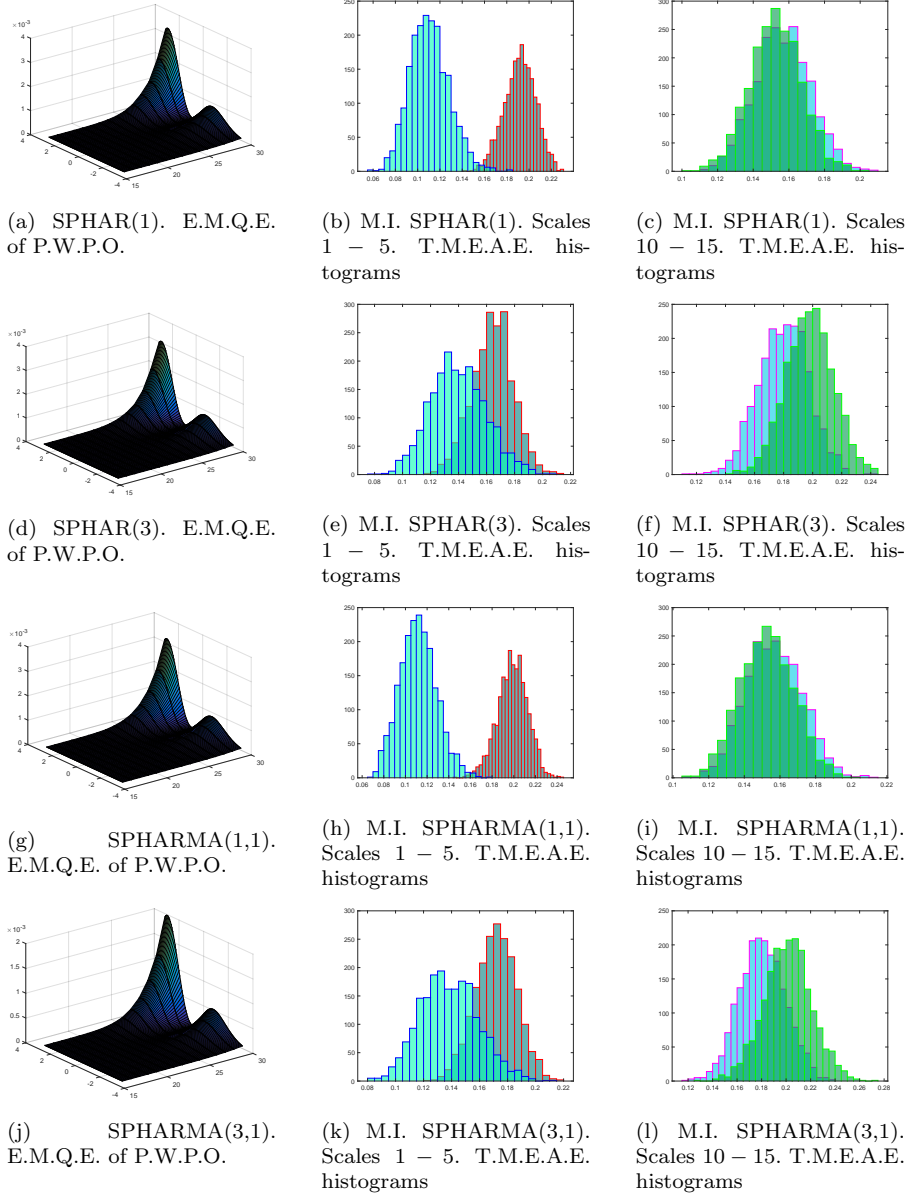(l) M.I. SPHARMA(3,1). Scales 10 − 15. T.M.E.A.E. histograms

Fig. 36: For the four families of multifractionally integrated functional spherical processes, the empirical mean quadratic errors associated with the weighted periodogram operator estimator, from projection into the eigenspaces H_n, $n = 16, \ldots, 30$, of the spherical Laplace Beltrami operator, are displayed (left–hand side). The bandwidth parameter $B_T = 0.1$ is chosen in all the cases. The remaining plots provide the histograms of the temporal mean of the empirical absolute errors, associated with the minimum contrast parameter estimation, from projection into the eigenspaces H_n, $n = 1, 5, 10, 15$, of the spherical Laplace Beltrami operator based on a functional sample size $T = 100$, and $R = 100$ repetitions

(a) SPHAR(1). E.M.Q.E. of P.W.P.O.

(b) M.I. SPHAR(1). Scales $1 - 5$. T.M.E.A.E. histograms

(c) M.I. SPHAR(1). Scales $10 - 15$. T.M.E.A.E. histograms

(d) SPHAR(3). E.M.Q.E. of P.W.P.O.

(e) M.I. SPHAR(3). Scales $1 - 5$. T.M.E.A.E. histograms

(f) M.I. SPHAR(3). Scales $10 - 15$. T.M.E.A.E. histograms

(g) SPHARMA(1,1). E.M.Q.E. of P.W.P.O.

(h) M.I. SPHARMA(1,1). Scales $1 - 5$. T.M.E.A.E. histograms

(i) M.I. SPHARMA(1,1). Scales $10 - 15$. T.M.E.A.E. histograms

(j) SPHARMA(3,1). E.M.Q.E. of P.W.P.O.

(k) M.I. SPHARMA(3,1). Scales $1 - 5$. T.M.E.A.E. histograms

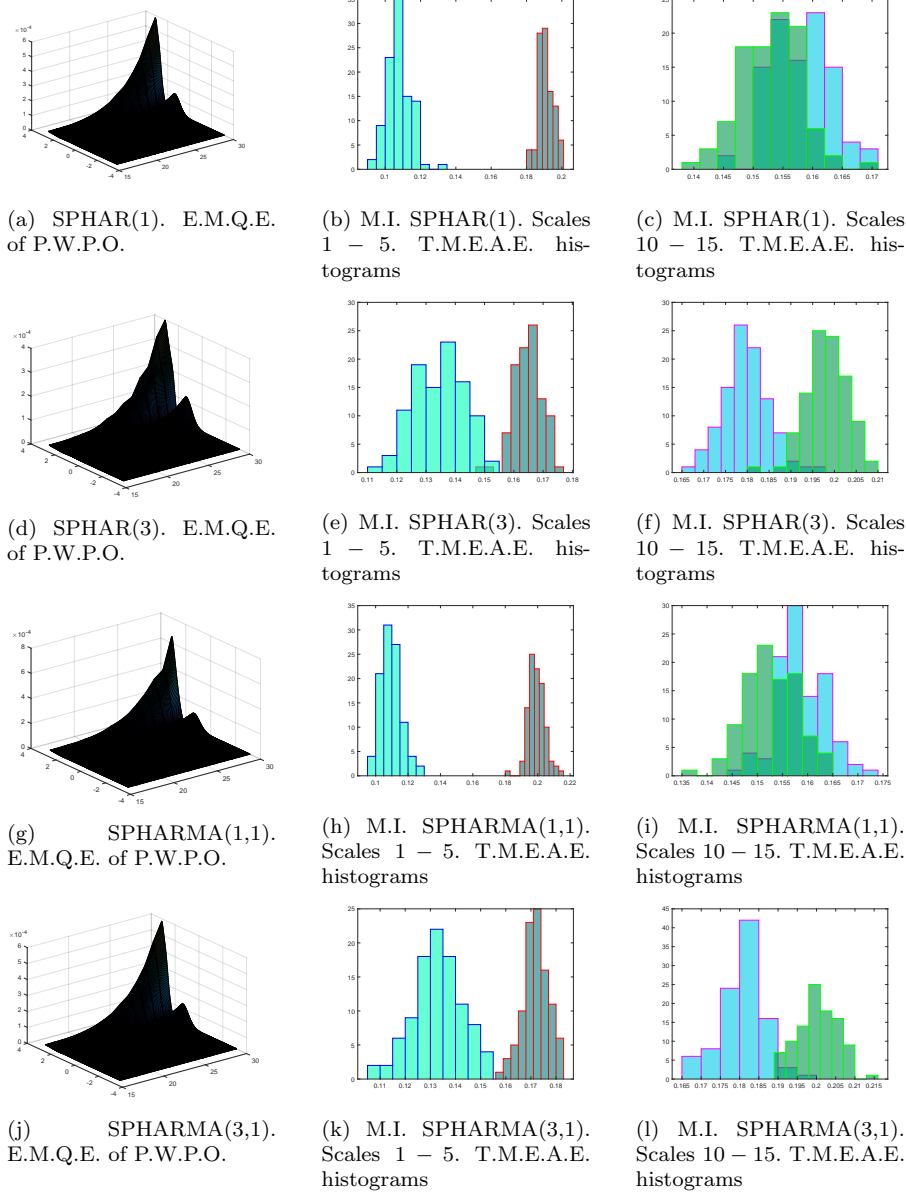(l) M.I. SPHARMA(3,1). Scales $10 - 15$. T.M.E.A.E. histograms

Fig. 37: For the four families of multifractionally integrated functional spherical processes, the empirical mean quadratic errors associated with the weighted periodogram operator estimator, from projection into the eigenspaces H_n, $n = 16, \ldots, 30$, of the spherical Laplace Beltrami operator, are displayed (left–hand side). The bandwidth parameter $B_T = 0.2$ has been chosen in all the cases. The remaining plots provide the histograms of the temporal mean of the empirical absolute errors, associated with the minimum contrast parameter estimation, from projection into the eigenspaces H_n, $n = 1, 5, 10, 15$, of the spherical Laplace Beltrami operator based on a functional sample size $T = 500$, and $R = 100$ repetitions

(a) SPHAR(1). E.M.Q.E. of P.W.P.O.

(b) M.I. SPHAR(1). Scales $1 - 5$. T.M.E.A.E. histograms

(c) M.I. SPHAR(1). Scales $10 - 15$. T.M.E.A.E. histograms

(d) SPHAR(3). E.M.Q.E. of P.W.P.O.

(e) M.I. SPHAR(3). Scales $1 - 5$. T.M.E.A.E. histograms

(f) M.I. SPHAR(3). Scales $10 - 15$. T.M.E.A.E. histograms

(g) SPHARMA(1,1). E.M.Q.E. of P.W.P.O.

(h) M.I. SPHARMA(1,1). Scales $1 - 5$. T.M.E.A.E. histograms

(i) M.I. SPHARMA(1,1). Scales $10 - 15$. T.M.E.A.E. histograms

(j) SPHARMA(3,1). E.M.Q.E. of P.W.P.O.

(k) M.I. SPHARMA(3,1). Scales $1 - 5$. T.M.E.A.E. histograms

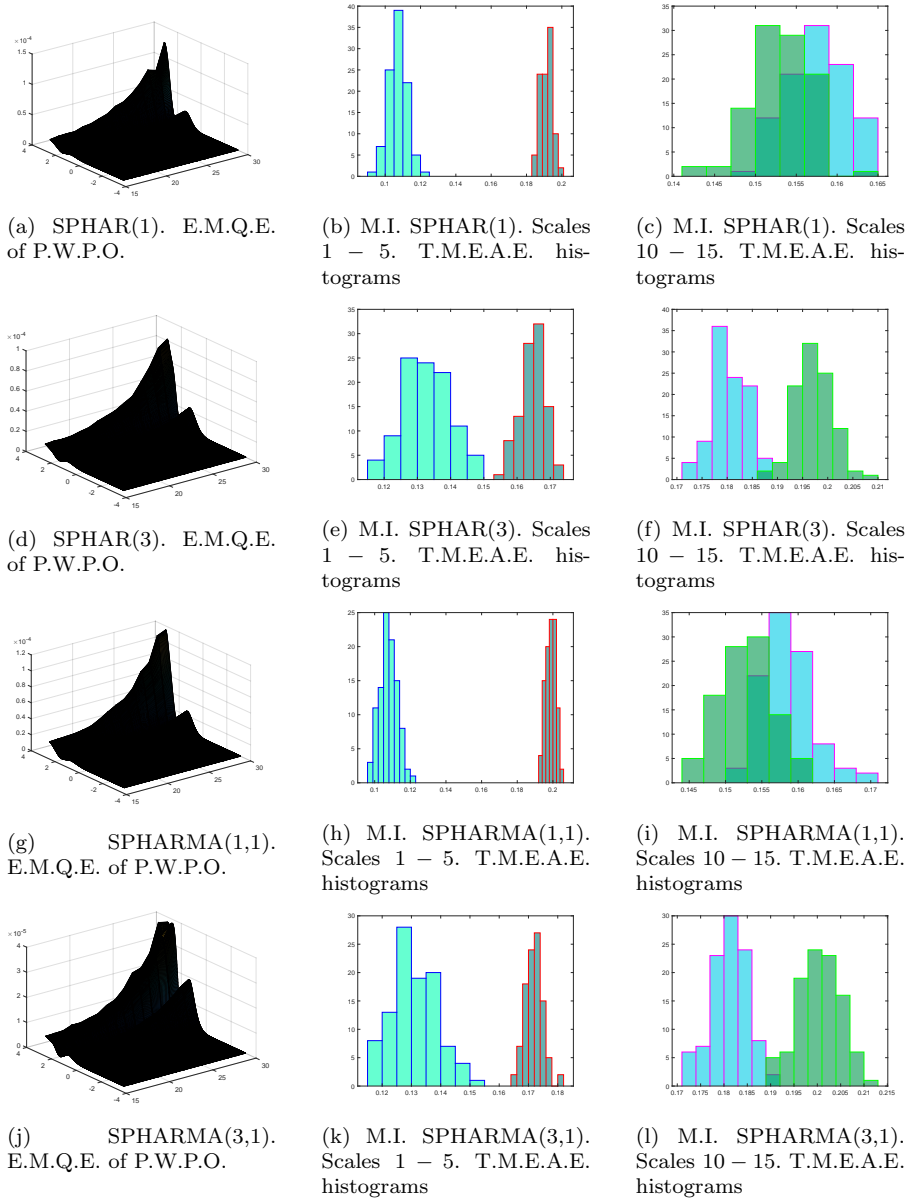(l) M.I. SPHARMA(3,1). Scales $10 - 15$. T.M.E.A.E. histograms

Fig. 38: For the four families of multifractionally integrated functional spherical processes, the empirical mean quadratic errors associated with the weighted periodogram operator estimator, from projection into the eigenspaces H_n, $n = 16, \ldots, 30$, of the spherical Laplace Beltrami operator, are displayed (left–hand side). The bandwidth parameter $B_T = 0.2$ has been chosen in all the cases. The remaining plots provide the histograms of the temporal mean of the empirical absolute errors, associated with the minimum contrast parameter estimation, from projection into the eigenspaces H_n, $n = 1, 5, 10, 15$, of the spherical Laplace Beltrami operator based on a functional sample size $T = 1000$, and $R = 100$ repetitions

6 Executing times

Tables 4 and 5 present the executing times of the implemented estimation algorithms for both, the minimum contrast (LRD operator), and SRD–LRD estimation methodologies under a specific model scenario. The computational cost, and timing consuming is very similar in all the models analyzed. In particular, the executing times for the multifractionally integrated SPHAR(1) process have been displayed. One can observe that the executing time of SRD–LRD estimation is significantly greater than the minimum contrast estimation when $R > 100$ for all T. In particular, for SRD–LRD estimation method, the capacity of the computer is not enough for executing $T = 500, R = 5000$ and $T = 1000, R = 2000, 5000$. Furthermore, one can observe that, in this estimation methodology, T is the dominant parameter affecting the SRD–LRD estimation results, since the threshold $R = 100$, where slight variations in the estimation results are observed when T is fixed and R is increasing. Hence, the results have been displayed for $R = 100$ in Section 5 of this Supplementary Materia.

Table 4: Executing times of minimum contrast estimation (LRD operator decreasing eigenvalues, multifractionally integrated SPHAR(1) process)

Functional sample size T	Repetitions R	Time (minutes)
	100	0.350
50	2000	0.619
	5000	0.987
	100	0.518
500	2000	1.123
	5000	1.937
	100	1.130
1000	2000	2.155
	5000	4.021

Table 5: Executing times of SRD–LRD estimation methodology (LRD operator decreasing eigenvalues (multifractionally integrated SPHAR(1) process), for $n = 1, \ldots, 15$, and SRD (SPHAR(1) process), for $n = 16, \ldots, 30$

Functional sample size T	Repetitions R	Time (minutes)
50	100	0.223
	2000	11.632
	5000	47.387
500	100	0.432
	2000	12.065
	5000	Out of memory
1000	100	0.780
	2000	Out of memory
	5000	Out of memory

References

Ma, C. and Malyarenko, A. (2020). Time varying isotropic vector random fields on compact two point homogeneous spaces. *J Theor Probab.* **33** 319–339.

Panaretos, V. M. and Tavakoli, S. (2013). Fourier analysis of stationary time series in function space. *Ann. Statist.* **41** 568–603.